Multiscale neural modeling of resting-state fMRI reveals executive-limbic malfunction as a core mechanism in major depressive disorder

Guoshi Li [a], Yujie Liu [a,b,c,d], Yanting Zheng [a,b,c,d], Ye Wu [a], Danian Li [e], Xinyu Liang [b], Yaoping Chen [b,f], Ying Cui [g], Pew-Thian Yap [a], Shijun Qiu [c,*], Han Zhang [a,1,*], Dinggang Shen [a,2,*]

[a] Department of Radiology and BRIC, University of North Carolina at Chapel Hill, Chapel Hill, NC USA
[b] The First School of Clinical Medicine, Guangzhou University of Chinese Medicine, Guangzhou, Guangdong, China
[c] Department of Radiology, The First Affiliated Hospital of Guangzhou University of Chinese Medicine, Guangzhou, Guangdong, China
[d] Department of Radiology, Guangzhou First People's Hospital, School of Medicine, South China University of Technology, Guangzhou, Guangdong, China
[e] Cerebropathy Center, The First Affiliated Hospital of Guangzhou University of Chinese Medicine, Guangzhou, Guangdong, China
[f] Department of Radiology, The Third Affiliated Hospital of Sun Yat-sen University, Guangzhou, Guangdong, China
[g] Cerebropathy Center, The Third Affiliated Hospital of Guangzhou Medical University, Guangzhou, Guangdong, China

ARTICLE INFO

ABSTRACT

Major depressive disorder (MDD) represents a grand challenge to human health and society, but the underlying pathophysiological mechanisms remain elusive. Previous neuroimaging studies have suggested that MDD is associated with abnormal interactions and dynamics in two major neural systems including the default mode - salience (DMN-SAL) network and the executive - limbic (EXE-LIM) network, but it is not clear which network plays a central role and which network plays a subordinate role in MDD pathophysiology. To address this question, we refined a newly developed Multiscale Neural Model Inversion (MNMI) framework and applied it to test whether MDD is more affected by impaired circuit interactions in the DMN-SAL network or the EXE-LIM network. The model estimates the directed connection strengths between different neural populations both within and between brain regions based on resting-state fMRI data collected from normal healthy subjects and patients with MDD. Results show that MDD is primarily characterized by abnormal circuit interactions in the EXE-LIM network rather than the DMN-SAL network. Specifically, we observe reduced frontoparietal effective connectivity that potentially contributes to hypoactivity in the dorsolateral prefrontal cortex (dlPFC), and decreased intrinsic inhibition combined with increased excitation from the superior parietal cortex (SPC) that potentially lead to amygdala hyperactivity, together resulting in activation imbalance in the PFC-amygdala circuit that pervades in MDD. Moreover, the model reveals reduced PFC-to-hippocampus excitation but decreased SPC-to-thalamus inhibition in MDD population that potentially lead to hypoactivity in the hippocampus and hyperactivity in the thalamus, consistent with previous experimental data. Overall, our findings provide strong support for the long-standing limbic-cortical dysregulation model in major depression but also offer novel insights into the multiscale pathophysiology of this debilitating disease.

1. Introduction

Major depressive disorder (MDD) is a serious mental illness that is characterized by depressed mood, diminished interests and impaired cognitive function (Otte et al., 2016). It is a leading cause of chronic disability worldwide with a lifetime prevalence of up to 17% (Kessler et al., 2005). Although the exact mechanisms underlying MDD remain unclear, functional magnetic resonance imaging (fMRI) has revealed systematic functional brain alterations in MDD (Menon, 2011; Otte et al., 2016; Lener et al., 2017). The first highly implicated large-scale

brain network is the default mode-salience network. The default model network (DMN) is activated in the resting brain and consists of ventral anterior cingulate cortex (vACC), posterior cingulate cortex (PCC)/precuneus, medial prefrontal cortex (mPFC), and lateral and inferior parietal cortex (Raichle, 2011; Dutta et al., 2014). The DMN has been implicated in rumination and self-referential processing (Cooney et al., 2010; Liston et al., 2014) and increased intrinsic connectivity in the DMN is hypothesized to underlie excessive self-focused rumination in MDD (Cooney et al., 2010; Hamilton et al., 2015). The salience (SAL) network, on the other hand, is activated in response to salient stimuli including emotional pain, empathy, metabolic stress and social rejection (Seeley et al., 2007; Hermans et al., 2014). Anchored in the dorsal anterior cingulate cortex (dACC) and anterior insula, the salience network is involved in integrating highly processed sensory information with visceral, autonomic and hedonic states, making it particularly important for interoceptive-autonomic processing (Seeley et al., 2007). Disruption of DMN-SAL connectivity has been reported in a number of MDD studies. Manoliu et al. (2014) found that MDD patients showed increased functional connectivity (FC) between DMN and SAL, consistent with greater resting-state FC between insula and anterior DMN (Avery et al., 2014). It has also been observed that FC between anterior DMN and SAL was positively correlated with depression severity in post-stroke depression (Balaev et al., 2018). Using dynamic causal modeling of rs-fMRI, we recently demonstrated that MDD was mainly associated with reduced effective connectivity within the DMN, and between the DMN and SAL networks (Li et al., 2020). These neuroimaging connectome studies support the notion that aberrant mapping or engagement of the DMN by SAL results in excessive rumination and abnormal interoceptive-autonomic processing in depression (Menon, 2011).

While recent studies focused on circuit disruption in the default mode and salience networks, it is not clear whether it is the cause of MDD pathology or just the consequence of a more fundamental neural mechanism. Indeed, both noninvasive and invasive brain stimulation such as transcranial magnetic stimulation (TMS) and deep brain stimulation (DBS) predominantly target the executive (e.g., dorsolateral prefrontal cortex) and limbic (e.g., thalamus) networks to relieve MDD symptoms (Leuchter et al., 2013; Delaloye and Holtzheimer, 2014; Liston et al., 2014; Raymaekers et al., 2017), suggesting the involvement of the executive-limbic system in MDD pathology. Opposite to the DMN, the executive control network (EXE) is most active during cognitive tasks (Seeley et al., 2007) and consists mainly of the dorsolateral prefrontal cortex (dlPFC) and posterior parietal cortex (PPC) (Corbetta and Shulman, 2002; Rogers et al., 2004; Seeley et al., 2007). The executive network plays a critical role in working memory maintenance, rule-based problem solving and decision-making during goal-directed cognitive tasks (Miller and Cohen, 2001; Petrides, 2005; Koechlin and Summerfield, 2007) as well as the regulation of emotional processing (Davidson et al., 2002; Phillips et al., 2008). The limbic (LIM) system, comprised of brain regions such as the amygdala, hippocampus and thalamus, underlies important brain functions including emotion, consciousness, motivation and long-term memory (LeDoux, 2000; Rolls, 2015). The involvement of the executive-limbic system in the pathophysiology of MDD has been well documented (Drevets et al., 2008; Disner et al., 2011; Pandya et al., 2012; Drysdale et al., 2017). Individuals with depression showed much more intense (up to 70%) and longer (up to three times) response in the amygdala than healthy subjects in response to negative stimuli (Drevets, 2001; Siegle et al., 2002). It has also been observed that the amygdala response in MDD patients increased linearly as the intensity of a sad facial expression increased (Surguladze et al., 2005). By comparison, the dlPFC exhibited lower response to negative stimuli in individuals with MDD than healthy subjects (Fales et al., 2008; Hamilton et al., 2012) and hypoactivation in the dlPFC was associated with excessive rumination (Ochsner et al., 2004; Ray et al., 2005). These studies suggest that insufficient control of the limbic system by the executive network results in aberrant emotional processing and depressive symptoms (Davidson et al., 2002; Beevers et al., 2010; Disner et al., 2011).

Although the two neurobiological models of depression (default mode-salience disruption versus executive-limbic malfunction) have each received considerable experimental support, their relative importance in MDD pathology has not been explicitly investigated. Addressing this question will shed light on the core neural circuitry mediating depression and the auxiliary circuitry that is likely subject to the influence of the core network, which can promote more targeting treatments. However, existing connectome studies of MDD have focused predominantly on undirected functional connectivity (i.e., statistical correlation) or graph theory of fMRI blood-oxygen-level-dependent (BOLD) signals (Gong and He, 2015; Kaiser et al., 2015), which cannot offer a neurophysiological account of the aberrant neural process. Effective connectivity (EC), by comparison, builds on generative models of neural interactions (Friston, 2011) and thus can, in principle, provide hidden neuronal mechanisms underlying observed fMRI data (Frässle et al., 2017). As a predominant approach to compute EC, Dynamic Causal Modeling (DCM) (Friston et al., 2003) has been applied to identify impaired inter-regional causal interactions in MDD based on either task-based (Almeida et al., 2009, 2011; Lu et al., 2012; Schlösser et al., 2008) or resting-state (Hyett et al., 2015; Li et al., 2017b; Kandilarova et al., 2018; Li et al., 2020) fMRI. Nevertheless, the underlying neural model of DCM for fMRI largely relies on a simplified linear state-space model for generating neural activity (Friston et al., 2003, 2014), which cannot capture impaired neural interactions at finer cellular and circuit levels.

To overcome the aforementioned limitations of traditional FC and EC studies, we have previously developed a Multiscale Neural Model Inversion (MNMI) framework that can link *mesoscale* intra-regional circuit interactions with *macroscale* inter-network dynamics and enable the estimation of both intra-regional and inter-network EC based on rs-fMRI (Li et al., 2019). Nevertheless, as a preliminary study, we estimated the EC among different functional networks instead of different brain regions due to the scale limit (i.e., the inter-regional EC was restricted to inter-network EC to reduce the freely estimable parameters), which may preclude the detection of more subtle EC change at single region level (i.e., between a pair of regions). In addition, the inter-network EC was assumed to be positive (excitatory), which cannot account for the potentially inhibitory effect between certain brain regions (e.g., the inhibitory effect from PFC to amygdala, Quirk et al., 2003). Here, we refined the MNMI framework by not only enabling inter-regional EC estimation but also relaxing the positive constraint on inter-regional EC. Notably, we came up with a structural connectivity (SC)-based method to reduce the number of inter-regional connections to those with strong SC to avoid the problem of over-fitting and improve estimation efficiency for more comprehensive and realistic modeling. By applying the refined MNMI approach to a relatively large rs-fMRI dataset consisting of 98 healthy normal control (NC) subjects and 96 individuals with first-episode drug-naïve (FEDN) MDD, we tested whether FEDN MDD is better characterized by default mode-salience or executive-limbic disruption. Results showed that MDD is primarily characterized by abnormal circuit interactions in the executive-limbic network rather than the default mode – salience network. Based on the findings, we proposed a neurophysiological model of executive – limbic malfunction that potentially explains depressive symptoms and pathology in MDD. Our study suggests that future treatments should specifically target the executive-limbic system for maximal therapeutic benefits.

2. Materials and Methods

2.1. Overview of the MNMI framework

The schematic diagram of the MNMI framework is depicted in Fig. 1. Each brain region consists of one excitatory and one inhibitory neural populations whose intrinsic dynamics are modeled using the biologically motivated Wilson-Cowan oscillators (Wilson and Cowan, 1972).
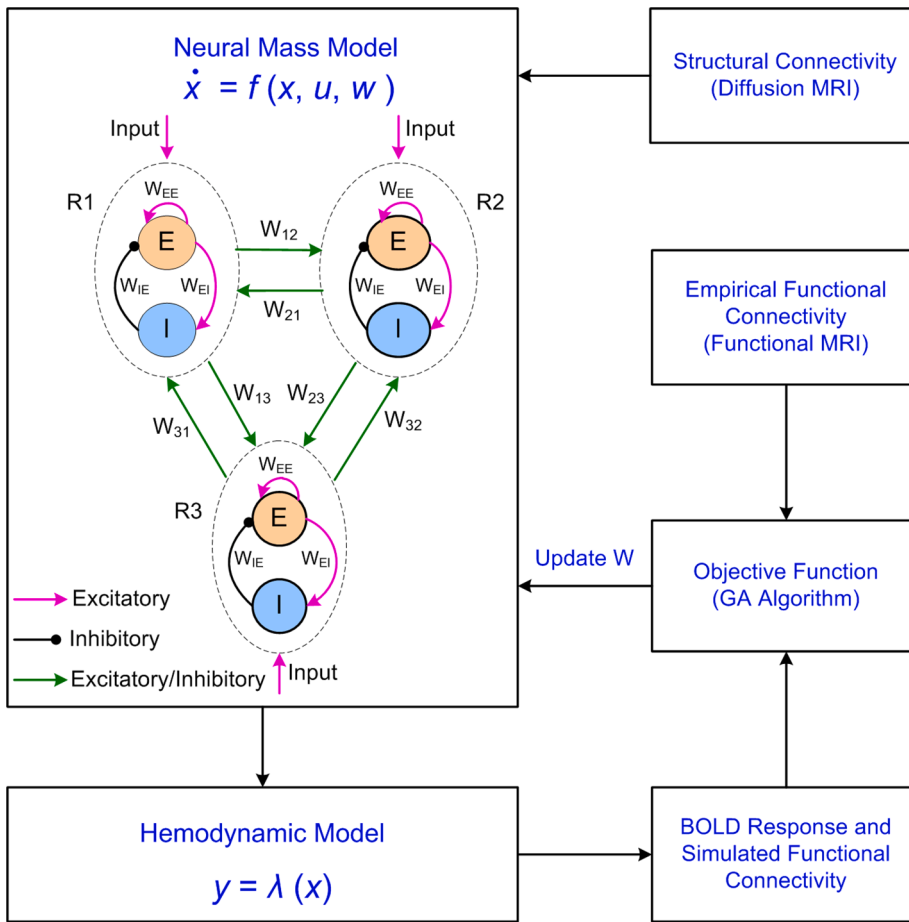
Fig. 1. A multiscale neural model inversion (MNMI) framework to estimate both intra-regional and inter-regional effective connectivity based on diffusion MRI and resting-state fMRI data. The neural activity is generated by a neural mass model consisting of multiple brain regions (R1, R2, R3, etc). Each brain region contains one excitatory (E) and one inhibitory (I) neural populations coupled with reciprocal local connections. The excitatory neural population excites the inhibitory neural population while receiving feedback inhibition from the latter as well as recurrent excitation from itself. Different brain regions are connected via long-range fibers whose baseline connection strength is determined by structural connectivity based on diffusion MRI. The neural activity is converted into corresponding BOLD signal via a biophysical hemodynamic model and the simulated functional connectivity (FC) is computed. The objective function is calculated as the opposite of the Pearson's correlation between the empirical and functional FC which is minimized by the genetic algorithm (GA). The model parameters (both local and inter-regional connection strengths) are updated iteratively until convergence is achieved.

The excitatory neural population excites the inhibitory neural population and receives feedback inhibition from the inhibitory population as well as recurrent excitation from itself. The excitatory neural populations within different brain regions are interconnected via long-range SC links consisting of white-matter fibers whose baseline connection strength is determined by diffusion tractography from diffusion MRI. The simulated neural activity is converted to simulated rs-fMRI BOLD signal through a biophysical hemodynamic model (Friston et al., 2003) and the corresponding FC matrix is constructed. Then, genetic algorithm, a biologically inspired optimization algorithm, is applied to estimate both local (intra-regional) and long-range (inter-regional) ECs in order to minimize the difference between the simulated and empirical FC matrices. Compared to the previous version of the MNMI framework (Li et al., 2019), the major changes included: 1) Inter-regional instead of inter-network ECs are separately estimated; 2) Inter-regional EC can be either positive (excitatory) or negative (inhibitory); 3) The optimization algorithm is changed from the Expectation-Maximization algorithm to the Genetic Algorithm; 4) a further expanded simulation length of the neural/BOLD activity (from 80 s to 200 s); and 5) a SC-guided inter-regional EC estimation where only strong inter-regional connections are allowed in the model. We applied the significantly refined MNMI model to two highly implicated neural systems in MDD pathology including the default mode – salience network and the executive – limbic network. Our main goal is to test which neural system underlies the more fundamental pathophysiological mechanism of MDD.

2.2. Subjects

We used the same fMRI dataset as our previous study (Li et al., 2020) except excluding two NCs and four MDDs who had excessive head

motion (mean frame-wise displacement (FD) (Power et al., 2012) is more than three time the standard deviation from the mean of their respective population), resulting in 98 NC and 96 MDD subjects. The FEDN patients were recruited from the psychological counseling outpatient of the First Affiliated Hospital of Guangzhou University of Chinese Medicine, Guangdong, China from September 2015 to June 2018. The MDD diagnosis was carried out by two experienced professional psychologists according to the 17-item Hamilton Rating Scale for Depression (HDRS-17, Hamilton, 1967) and the Diagnostic and Statistical Manual 5th edition (DSM-5, American Psychiatric Association, 2013). The selected FEDN patients were right-handed native Chinese speakers aged between 18 and 55 years old who were firstly diagnosed with MDD and had no history of any neurological illness or any other forms of psychiatric disorders. The healthy subjects were enrolled locally during the same period of time and were physically and mentally healthy based on their medical history and the Mini-International Neuropsychiatric Interview (Sheehan et al., 1998) with a total HDRS-17 score of less than seven. The study was approved by the ethics committee of The First Affiliated Hospital of Guangzhou University of Chinese Medicine and all participants provided written informed consent complying with the Declaration of Helsinki.

2.3. FMRI acquisition and preprocessing

The MRI acquisition was based on a 3.0-T GE Signa HDxt scanner with an 8-channel head-coil within three days of diagnosis and the preprocessing procedures were detailed in Li et al. (2020) and briefly described as follows. The acquisition parameters for the rs-fMRI were: TR (repetition time) = 2000 ms, TE (echo time) = 30 ms, flip angle = 90°, matrix size = 64 × 64, and slice spacing = 1.0 mm, and those for the

structural MRI were: slice thickness = 1.0 mm (156 slices), no slice gap, matrix = 256 × 256, field of view = 256 × 256 mm². Image pre-processing was performed using SPM12 (www.fil.ion.ucl.ac.uk/spm) and Data Processing Assistant for Resting-State fMRI (DPARSF) version 2.3 (http://rfmri.org/DPARSF) (Yan and Zang, 2010). For each subject, 180 rs-fMRI volumes were remained after removing the first five volumes. The remaining images were corrected for slice acquisition timing and head motion. The structural MRI was used to guide rs-fMRI registration by using unified segment and Diffeomorphic Anatomical Registration through Exponentiated Lie Algebra (DARTEL). The rs-fMRI data was smoothed with a 6-mm full-width-at-half-maximum (FWHM) Gaussian kernel and denoised by regressing out several nuisance signals, including the Friston-24 head motion parameters and signals from cerebrospinal fluid and white matter, followed by linear detrending and temporal band-pass filtering (0.01–0.08 Hz).

2.4. Structural connectivity

To introduce structural constraint on EC, structural connectivity was assessed based on probabilistic tractography with the diffusion MRI data from the Human Connectome Project. Data from 14 unrelated and randomly selected subjects was processed and the resulting SC matrices were averaged. Specifically, for each of the 14 subjects, tissue segmentation was performed on the structural MRI (aligned with the diffusion MRI data) from the 14 subjects based on FreeSurfer (https://surfer.nmr.mgh.harvard.edu/) according to the pipeline described in Smith et al. (2012). After minimal preprocessing of the diffusion MRI data, probabilistic tractography was employed in the diffusion MRI's native space using the first-order integration over fiber orientation distributions (iFOD1) algorithm estimated by spherical deconvolution approach that considered fiber crossing (Tournier et al., 2010) to reconstruct two million streamlines within the whole brain with random seeds. The output streamlines were cropped at the grey matter-white matter interface with a search distance of 2 mm, where the Destrieux atlas (included with FreeSurfer; Destrieux et al., 2010) that contains 164 regions of interest (ROIs) was applied, resulting in a 164 × 164 SC matrix. Each element of SC represented the number of streamlines between a pair of ROIs which was normalized by the average volume of them. Based on the full SC matrix, we sampled the SC matrices for the DMN-SAL network and the EXE-LIM network separately. They were further normalized by the maximal entry of the two matrices so the SC was bounded between 0 and 1.

2.5. Functional connectivity

From the Destrieux atlas, we selected 16 key ROIs (Table 1) for the four functional networks (DMN, SAL, EXE and LIM; see **Introduction** section). These ROIs are visualized in Fig. 2. Of note, more ROIs could be easily included as a natural extension of our method in the future. The DMN-SAL network included seven ROIs: ventral anterior cingulate cortex (vACC, combining both left and right portion of it since it is in the medial part of the brain, similarly for other midline brain regions unless specified otherwise), posterior cingulate cortex (PCC, both ventral and dorsal parts), and left and right lateral parietal cortices (LPC, each side represents one ROI) from DMN, as well as dorsal anterior cingulate cortex (dACC), and left and right insula from SAL. The EXE-LIM network contained nine ROIs: left and right dorsolateral prefrontal cortices (dlPFC), and left and right superior parietal cortices (SPC) from EXE, as well as the thalamus, left and right amygdala, and left and right hippocampus from LIM. Since the brain parcellation was carried out by Freesurfer in each subject's native space, to apply those ROIs to the preprocessed rs-fMRI data in the MNI space, we used *FNIRT* in FSL (https://fsl.fmrib.ox.ac.uk/fsl) to estimate the deformation field based on each subject's structural MRI after it was aligned to the same subject's rs-fMRI, which generated the transformation from the native structural MRI space to the standard MNI space. This transformation was

Table 1
ROI definitions of the default mode-salience and executive-limbic networks with corresponding index numbers in the Destrieux atlas included in FreeSurfer.

Region name (abbr.)		Index # (FreeSurfer)
DMN-SAL Network		
DMN		
1	Ventral anterior cingulate cortex (vACC)	6 & 95
2	Posterior cingulate cortex (PCC)	9, 10 & 98, 99
3	Left lateral parietal cortex (L.LPC)	25
4	Right lateral parietal cortex (R.LPC)	114
SAL		
5	Dorsal anterior cingulate cortex (dACC)	7 & 96
6	Left insula	18
7	Right insula	107
EXE-LIM Network		
EXE		
1	Left dorsolateral prefrontal cortex (L.dlPFC)	52
2	Right dorsolateral prefrontal cortex (R.dlPFC)	141
3	Left superior parietal cortex (L.SPC)	27
4	Right superior parietal cortex (R.SPC)	116
LIM		
5	Thalamus (Thal)	76 & 83
6	Left amygdala (L.Amyg)	81
7	Right amygdala (R.Amyg)	88
8	Left hippocampus (L.HPC)	80
9	Right hippocampus (R.HPC)	87

Abbreviations: DMN: default mode network; SAL: salience network; EXE: executive network; LIM: limbic network

then used to warp the partitions from the native structural MRI space to the rs-fMRI space. Regional averaged BOLD rs-fMRI time series were extracted from the 16 ROIs and, the FC matrix was calculated using Pearson's correlation. To estimate more accurate FC by removing the effect of potential noise and artifacts, we divided the total 360-s BOLD time series into ten 180-s sliding windows with an interval of 20 s. The final FC was computed by averaging the ten corresponding FC matrices after removing the outliers (more than three scaled median absolute deviations away from the median) for each FC link (i.e., FC matrix element).

2.6. Network modeling of neural activity

We applied computational neuronal modeling to capture neural interactions both within and between brain regions. Each brain region consisted of reciprocally coupled excitatory and inhibitory neural populations (Fig. 1). The regional brain dynamics was simulated by a neural mass model using the biologically motivated nonlinear Wilson-Cowan oscillator (Wilson and Cowan, 1972). The population-level activity of the jth region was governed by the following two equations (Abeysuriya et al., 2018):

$$\tau_e \frac{dE_j(t)}{dt} = -E_j(t) + S\left(\sum_k C_{kj} W_{kj} E_k(t) + W_{EE} E_j(t) - W_{IE} I_j(t) + u + \varepsilon(t)\right) \tag{1}$$

$$\tau_i \frac{dI_j(t)}{dt} = -I_j(t) + S\left(W_{EI} E_j(t) + \varepsilon(t)\right) \tag{2}$$

where E_j and I_j are the mean firing rates of the excitatory and inhibitory neural populations in brain region j, τ_e and τ_i are the excitatory and inhibitory time constants (20 ms; Hellyer et al., 2016), W_{EE}, W_{EI} and W_{IE} are the local connection strengths from excitatory to excitatory neural population, from excitatory to inhibitory neural population and from inhibitory to excitatory neural population, respectively. The variable u is a constant external input, and $\varepsilon(t)$ is random additive noise following a normal distribution centering at 0 with standard deviation of 0.3. It is important to mention that the constant input u and noisy input $\varepsilon(t)$ represent the extrinsic inputs from other un-modeled brain regions to allow the generalization ability of the model (Deco et al., 2013b; Wang
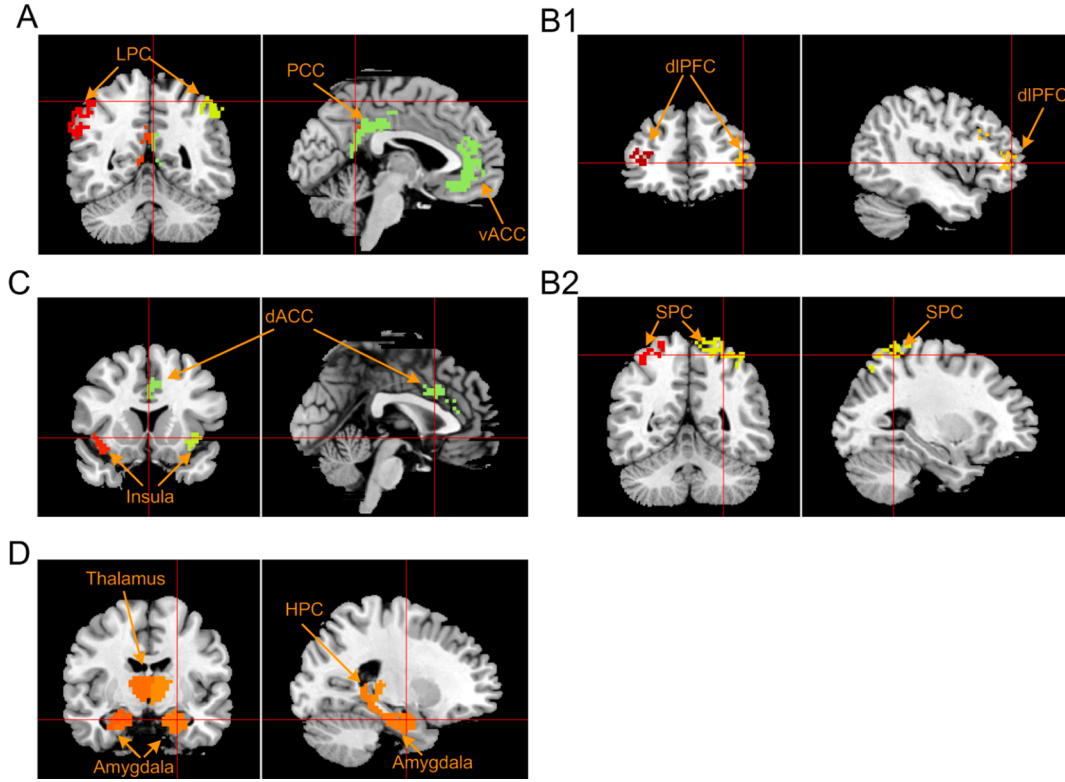
Fig. 2. Regions of interest (ROIs) included in the MDD model. (A) ROIs in the default mode network. (B) ROIs in the executive control network. (C) ROIs in the salience network. (D) ROIs in the limbic network. vACC: ventral anterior cingulate cortex, PCC: posterior cingulate cortex, LPC: lateral parietal cortex, dlPFC: dorsal lateral prefrontal cortex, SPC: superior parietal cortex, dACC: dorsal anterior cingulate cortex, HPC: hippocampus.

et al., 2019). The long-range connectivity strength from region k to region j is represented by W_{kj} (and that from region j to k is W_{jk}) that was derived from empirical SC and scaled by an inter-regional coupling factor C_{kj} to model individual difference. The nonlinear response function S is modeled as a sigmoid function $S = 1/(1 + e^{-(\frac{x-\mu}{\sigma})})$ (μ=1.0; σ = 0.25; Abeysuriya et al., 2018).

2.7. Hemodynamic modeling

The neural activity of each brain region was converted into corresponding BOLD signal using a well-established hemodynamic model (Friston et al., 2003). Specifically, for each region j, the fluctuation in neuronal activity x_j (E_j and I_j) gives rise to a vasodilatory signal s_j that is subject to self-regulation. The vasodilatory signal causes change in the blood flow f_j leading to subsequent change in blood volume v_j and deoxyhemoglobin content q_j. The hemodynamic state equations with parameters are given by:

$$\frac{ds_j}{dt} = x_j - \kappa s_j - \gamma(f_j - 1) \tag{3}$$

$$\frac{df_j}{dt} = s_j \tag{4}$$

$$\tau \frac{dv_j}{dt} = f_j - v_j^{1/\alpha} \tag{5}$$

$$\tau \frac{dq_j}{dt} = \frac{f_j}{\rho}\left[1 - (1-\rho)^{1/f_j}\right] - \frac{q_j}{v_j}v_j^{1/\alpha} \tag{6}$$

where κ is the rate of decay (0.65 per second), γ is the rate of flow-dependent elimination (0.41 per second), τ is the hemodynamic transit time (0.98 s), α is the Grubb's exponent (0.32) and ρ is the resting oxygen extraction (0.34). The neural activity from excitatory and

inhibitory populations is summed up within each region with respective weighting (2/3 for excitatory and 1/3 for inhibitory; Becker et al., 2015) to obtain the overall regional neural activity x_j. The simulated BOLD signal is taken to be a static nonlinear function of volume and deoxyhemoglobin that depend on the relative contribution of intravascular and extravascular components:

$$y_j = v_0(k_1(1-q_j) + k_2(1-q_j/v_j) + k_3(1-v_j)) \tag{7}$$

where v_0 is the resting blood volume fraction (0.02), and k_1, k_2 and k_3 are the intravascular, concentration and extravascular coefficients, respectively ($k_1 = 7\rho$, $k_2 = 2$, and $k_3 = 2\rho - 0.2$).

2.8. Numerical integration

The Wilson-Cowan and hemodynamic models were simulated using the 4th order Runge-Kutta (RK) scheme (Abeysuriya et al., 2018) with an integration step of 10 ms (Wang et al., 2019); shorter integration step had no significant effect on the results reported. We simulated the network for a total of 200 s, and the first 20 s of the BOLD activity was discarded to remove transient effects. The remaining 180-s (3-min) time series were downsampled to 0.5 Hz to have the same temporal resolution as the real, recorded BOLD rs-MRI signals.

2.9. Estimation of model parameters

The free parameters in the neural network model included both local (intra-regional) and long-range (inter-regional) ECs. For the local parameters, we estimated both the recurrent excitation (W_{EE}, excitatory to excitatory) and recurrent inhibition (W_{IE}, inhibitory to excitatory) weights in each brain region. The excitatory to inhibitory weight (W_{EI}) was assumed to be constant and equaled to three (Abeysuriya et al., 2018) as the effect of W_{EI} could be accommodated by the change in W_{IE}.

The inter-regional coupling factor C_{kj} was also estimated in the neural mass model. As mentioned, the DMN-SAL network contained seven ROIs and the EXE-LIM network consisted of nine ROIs, which gave rise to 42 and 72 inter-regional connections, respectively (diagonal connections were excluded as we estimated recurrent excitation and inhibition separately; Demirtaş et al., 2019). To improve model estimation accuracy and efficiency, we performed one sample *t*-test on each structural connection link across the 14 subjects from the Human Connectome Project and only preserved the links with strong SC ($p < 0.0001$, uncorrected). The threshold was chosen so that about half of the (weaker) inter-regional connections were removed for either network while neither network would have more than half of the connections removed. We performed SC thresholding due to two important reasons. First, SC pruning is needed to remove invalid connections. It is well known that diffusion tensor imaging (DTI) based tractography is subject to noise and could contain invalid bundles even though there are no true fiber connections (Maier-Hein et al., 2017). To avoid false positive connections, it is reasonable to remove weak SC connections. Second, SC pruning is necessary to avoid overparameterization and enable more accurate EC estimation. As the number of inter-regional EC parameters increases exponentially with the number of brain regions, it could lead to potential problems of overfitting. Such problems can be eased by removing weak SC links (most likely due to noise) in the model. It is noted that pre-estimation EC pruning has been implemented in connectome modeling such as spectral DCM which uses FC to place shrinkage priors on implausible effective connections (Razi et al., 2017). Our method differs from spectral DCM in that we use SC instead of FC to constrain the number of EC parameters. Practically, it assumes that the (direct) EC (between two brain regions) is zero in the absence of a direct SC link, although indirect or high-order EC may still exist due to polysynaptic influences (Sokolov et al., 2020). Using the SC pruning strategy, twenty links were removed from each of the DMN-SAL and EXE-LIM networks, resulting in 22 and 52 inter-regional connections for the two much sparser networks, respectively. In addition, the external input (u) was also estimated and assumed to be identical for all brain regions of a subject. Consequently, a total of 37 (14 local, 22 inter-regional, and one for shared external input) parameters were estimated for the DMN-SAL network and a total of 71 (18 local, 52 inter-regional, and one for shared external input) parameters were estimated for the EXE-LIM network.

We used the genetic algorithm (function *"ga"*) contained in the MATLAB's global optimization toolbox to estimate the model parameters. Genetic algorithm (GA) is a biologically inspired method for solving both constrained and unconstrained optimization problems based on natural selection, the process that drives biological evolution (Mitchell, 1995). GA repeatedly modifies a population of individual solutions. At each step, it selects individuals at random from the current population to be parents and uses them to produce the children for the next generation. Over successive generations, the population "evolves" toward an optimal solution. GA differs from other regular optimization algorithms in that it generates a population of points (instead of a single point) at each iteration and uses stochastic (instead of deterministic) computation to select the next population, which is suitable for optimization problems involving discontinuous, non-differentiable, stochastic or highly nonlinear objective functions. When using the "ga" function in MATLAB, initial conditions of the free parameters are not needed but parameters can be constrained within a prescribed range. In the MNMI framework, the free parameters were bounded within certain ranges to achieve balanced excitation and inhibition in the network; those ranges were selected based on previous modeling work as well as extensive simulations to avoid excessive network excitation or inhibition. Based on a previous model (Abeysuriya et al., 2018), we assumed a default value of 3.0 for both recurrent excitation (W_{EE}) and inhibition (W_{IE}) strengths, and a default value of 0.3 for the external input (u). Therefore, we set the searching ranges around the default values, i.e., [2.0 4.0] for both recurrent excitation and inhibition weights, and [0.2 0.4] for the external input, by allowing a maximum of 33.3% variation from the

default value. We allowed the inter-regional connection weight to be either positive (excitatory) or negative (inhibitory), so we set the searching range to be [-2.0 2.0] for the inter-regional coupling factor (C_{kj}). This allows a relatively wide range for inter-regional EC weight, but at the same time, avoids unconstrained parameter estimation that could generate extreme and unrealistic estimates. Note that we assumed the inter-regional inhibition could occur directly between excitatory neural populations (instead of via local inhibitory neurons) for simplicity.

We set the objective function to be the distance, measured by the opposite of the Pearson's correlation, between the simulated and empirical FC matrices, so that the genetic algorithm could maximize the Pearson's correlation between the simulated and empirical FC for each subject. The tolerance was set to be 0.001 and the maximal number of generations was set to be 128. We observed good convergence within 128 generations for all the subjects and an even smaller tolerance did not change the estimated parameters in any significant way. The genetic algorithm repeatedly generated a population of solutions (or parameter set) based on stochastic computation in each iteration and evaluated the objective function by numerically integrating the neural mass and hemodynamic models (for each parameter set) until the average change in the fitness value (the value of the objective function) was less than the functional tolerance. The entire MNMI optimization procedure with model integration was coded with MATLAB (R2018b) and run at a Linux-based high-performance cluster. The genetic algorithm program was run in parallel with 12 cores using the Parallel Computing Toolbox in MATLAB. The typical computing time (for each individual subject) ranged from 10 to 20 h for the DMN-SAL network and 12 to 30 h for the EXE-LIM network with a few subjects taking more than 30 h.

2.10. Ground-truth simulation

To assess the face validity of MNMI, we generated 20 new synthetic individuals for each of the DMN-SAL and EXE-LIM networks for which the ground truth (i.e., the parameter values) was known (Frässle et al., 2017). To ensure the data were realistic, we randomly sampled model parameters from the parameter distributions estimated from the full dataset (i.e., N = 194 subjects), as a previous study (Singh et al., 2020). More specifically, the mean and standard deviation of each free parameter (37 for DMN-SAL and 71 for EXE-LIM) were estimated first from the full dataset (i.e., empirical models were inverted first). The corresponding ground-truth parameter was then drawn from the normal distribution with the estimated mean and standard deviation. If a randomly selected ground-truth parameter exceeded the upper bound or fell below the lower bound as specified above, it was set to the upper bound or lower bound. With selected ground-truth parameters, the neural mass and hemodynamic models were simulated as described above to generate synthetic BOLD time series (180 s with TR = 2 s). For sensitivity analysis, the final simulated BOLD signal was added white gaussian noise with zero mean to model the measurement error (Frässle et al., 2017; Singh et al., 2020). Based on previous definition of signal-to-noise ratio (SNR; Frässle et al., 2017), we introduced noise-to-signal ratio (NSR) as the ratio between standard deviation of the noise and standard deviation of the BOLD signal (i.e., $NSR = \sigma_{noise}/\sigma_{signal}$). We systematically varied the NSR from 0 to 0.5 with a step of 0.1 and computed the simulated FC using Pearson's correlation. The synthetic FC was then used as input to the MNMI to estimate ground-truth parameters.

2.11. Statistical analysis

The model parameters were estimated for each subject and compared between the NC and MDD groups. We used a two-sample *t*-test to compare each of the estimated model parameters and the significant level was set to a false discovery rate (FDR; Benjamini and Yekutieli, 2001) of $q < 0.05$. We also reported the Cohen's d effect size which is

determined by calculating the mean difference between the NC and MDD groups, and then dividing the result by the pooled standard deviation. We did not use network-based statistics (NBS, Zalesky et al., 2010) as our previous study (Li et al., 2020) did because we estimated both intra- and inter-regional EC and we removed weak inter-regional connections making it difficult to fulfill the topological cluster requirement of NBS.

2.12. Data and code availability

The data and code that support the findings of this study are available from the GitHub repository at https://github.com/Guoshi-Li/ MNMI_MDD. The structural and diffusion MRI data for the 14 subjects used to construct SC was randomly selected from the WU-Minn HCP Dataset (1200 subjects) available from the Connectome Database (https://db.humanconnectome.org/). All structural and functional connectivity matrices along with BOLD fMRI time series are available from the GitHub repository given above.

3. Results

3.1. Participants

The demographic and clinical characteristics of the participants are shown in Table 2. There was no significant difference in age ($p = 0.99$, two-sample t-test), gender ($p = 0.35$, chi-square test), or education ($p = 0.34$, two-sample t-test) between the NC and MDD groups. The disease duration was 8.76 ± 11.04 months, and the HDRS-17 score was 22.08 ± 3.10 for the MDDs.

3.2. Model parameter estimation with synthetic data

Model inversion with MNMI requires a baseline SC matrix (Fig. 1). The SC matrices of the DMN-SAL network and EXE-LIM network derived from diffusion MRI are shown in Fig. 3A, B, respectively. In the DMN-SAL network, the strongest connections existed between vACC/PCC and dACC followed by the connections between vACC and PCC. In the EXE-LIM network, relatively high level of connections appeared between left and right SPC, thalamus and SPC, thalamus and hippocampus, and amygdala and hippocampus. According to the one-sample t-test results, strong links were preserved (green edges in Fig. 3C, D) while the remaining connections were removed.

We first conducted ground-truth simulations to evaluate the face validity of MNMI by generating 20 synthetic subjects for the DMN-SAL network and EXE-LIM network respectively (see Materials and Methods). After optimization, the simulated FC closely matched the ground-truth FC for both networks (Supplemental Fig. S1). Indeed, the average fitness value (measured by Pearson's correlation between the simulated and ground-truth FC matrices) was 0.98 ± 0.03 for the DMN-SAL network and 0.97 ± 0.02 for the EXE-LIM network. By maximizing the similarity between simulated and ground-truth FC, MNMI was able to recover the ground-truth parameters with relatively high accuracy at

individual subject level for both networks (Supplemental Fig. S2). The population-averaged ground-truth and estimated EC parameters are shown in Fig. 4 (note that recurrent inhibition weight is shown positive due to the preceding negative sign in Eqn (1)). We observed that the estimated parameters were similar to the ground-truth parameters at the population level in that most of EC estimations followed the sign and amplitude of the ground-truth parameters in a close matter. Out of 36 EC parameters in the DMN-SAL network, only one parameter showed uncorrected significance ($p < 0.05$, uncorrected) between estimated and ground-truth EC (Fig. 4C). By comparison, out of 70 EC parameters in the EXE-LIM network, four parameters showed uncorrected significance between estimated and ground-truth EC (Fig. 4B, D). It should be noted that none of the difference could pass multiple correction, indicating that MNMI was able to faithfully recover the population EC mean. We next introduced white Gaussian noise into the simulated BOLD signal and assessed the sensitivity of parameter fitting to unmodeled measurement error. We varied the noise-to-signal ratio (NSR) from 0.1 to 0.5 (with a step of 0.1) and inverted the neural mass model using MNMI under each noise level for all 20 synthetic subjects for both networks. We then computed the Pearson's correlation between the estimated EC and ground-truth EC for all 20 synthetic subjects together as a function of NSR (Fig. 5). Expectedly, the correlation showed an overall decreased profile as the NSR increased, for both intra-regional and inter-regional EC (Fig. 5A, B). Specifically, the correlation coefficient (R) of the intra-regional EC decreased from about 0.5/0.4 (DMN-SAL/EXE-LIM) to about 0.3/0.2 while that of the inter-regional EC reduced from about 0.4/0.33 to about 0.2/0.22 as the NSR increased from 0 to 0.5. Notably, the correlation profile started to level off or even slightly increased when the NSR exceeded 0.3, suggesting the inherent robustness of MNMI to large measurement error. Such robustness may result from the fact that at high noise level the neural model inversion dynamics has reached a steady state and GA used stochastic computation to search for optimal solution, which can naturally handle large noise variation and enable stable parameter estimation. Also, we noted that for intra-regional EC, parameter fitting was better for the DMN-SAL network compared with the EXE-LIM network, while for inter-regional EC, the two networks had quite similar performance (compare Fig. 5A with Fig. 5B). As the EXE-LIM network contained almost twice the number of free parameters as the DMN-SAL network (71 vs. 37), it suggests that expansion of the network dimension would have a larger effect on the estimation accuracy of intra-regional EC. The associated p values displayed in Fig. 5C, D indicated that the correlation between estimated and ground-truth EC was highly significant ($p < 1e-5$) for low NSR (NSR < 0.3) and remained significant ($p < 0.005$) even for large NSR (NSR ≥ 0.3). Overall, the ground-truth simulation demonstrates that MNMI is able to recover the ground-truth parameters reasonably well and the estimation performance remains fairly stable to large variation of measurement noise.

3.3. MNMI performance with empirical data

After the MNMI framework was validated with synthetic data, we applied the method to empirical rs-fMRI dataset with 98 NC and 96 MDD subjects. As described in the Methods section, we fit the model parameters of both the DMN-SAL and EXE-LIM networks based on individual rs-fMRI data. By comparing the estimated EC parameters between NCs and MDDs for both networks, we aimed to identify disrupted connections in MDD and determine which network was more significantly impaired in FEDN-MDD. We observed that the GA converged within 128 iterations/generations for all subjects and within 80 generations for most of the subjects. Exemplary convergence curves for the DMN-SAL and EXE-LIM networks from a randomly selected NC subject are separately shown in Fig. 6A, B. The estimation converged rapidly within the first 20 generations and became relatively flat after 40 generations until convergence. The average model fitness value (measured by Pearson's correlation between the simulated and empirical FC matrices) was 0.92 for both NC and MDD in the DMN-SAL network ($p = 0.8$, two-sample t-
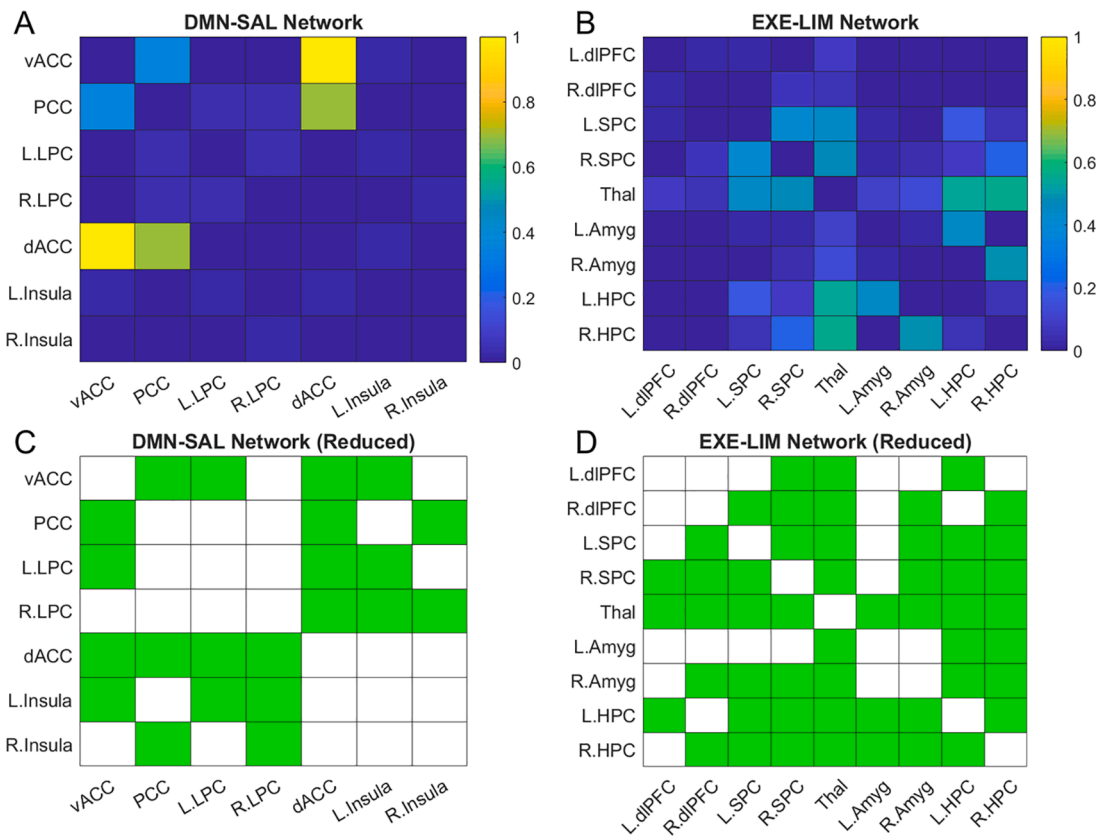
Table 2
Demographic and clinical characteristics of participants.

Characteristics	MDD (n = 96)	NC (n = 98)	$t/\chi2$	p
Age (years)	29.64 ± 9.51[a]	29.48 ± 10.29	-0.02	0.99[b]
Gender (F/M)	63/33	58/40	0.86	0.35[c]
Education (years)	12.51 ± 3.26	12.93 ± 2.77	-0.96	0.34[b]
Duration (months)	8.76 ± 11.04	NA	NA	NA
HDRS-17	22.08 ± 3.10	NA	NA	NA

Abbreviations: MDD, major depressive disorder; NC, normal control; HDRS-17, 17-item Hamilton Depression Rating Scale.
[a] Mean ± standard deviation.
[b] The p values were obtained by two-sample t-test.
[c] The p value was obtained by a chi-square test.

Fig. 3. Structure connectivity of the DMN-SAL network and the EXE-LIM network with corresponding reduced networks. (A) Normalized structure connectivity of the DMN-SAL network. (B) Normalized structure connectivity of the EXE-LIM network. (C) Reduced DMN-SAL network. (D) Reduced EXE-LIM network. Green edges indicate the connections that remain in the network. (For interpretation of the references to colour in this figure legend, the reader is referred to the web version of this article.)

test; Fig. 6C) and 0.87 for both NC and MDD in the EXE-LIM network ($p = 0.49$, two-sample t-test; Fig. 6D). Note that the model fitness value was considerably lower for empirical data compared with synthetic data (~0.98) because the synthetic data was generated by the neural mass model while there was considerable variance in empirical data. Also, the fitness value in the EXE-LIM network was significantly lower than that in the DMN-SAL network for both NC ($p < 0.05$, two-sample t-test; Cohen's d: -0.98) and MDD ($p < 0.05$, two-sample t-test; Cohen's d: -0.88) groups. Such difference largely reflected the fact that the dimension of the FC matrix in the EXE-LIM network (9×9) was larger than that in the DMN-SAL network (7×7). The simulated results for the DMN-SAL and EXE-LIM networks (using the optimized parameters) from a randomly selected NC subject are shown in Figs. 7 and 8, respectively. We found that the simulated neural activity and BOLD signals displayed rhythmic fluctuations in a fast and slow temporal scale, respectively. The average oscillation frequency of the simulated neural activity was about 7 Hz, which resembled alpha oscillations during relaxed wakefulness (Hughes and Crunelli, 2005). The oscillation frequency of the simulated BOLD signals ranged between 0.02 and 0.08 Hz, consistent with previous experimental observations (Tong et al., 2019). There was no significant difference between NC and MDD groups, for both DMN-SAL (NC: 0.06 ± 0.008 Hz; MDD: 0.06 ± 0.009 Hz, $p = 0.29$, two-sample t-test) and EXE-LIM networks (NC: 0.05 ± 0.013 Hz; MDD: 0.05 ± 0.013 Hz, $p = 0.74$, two-sample t-test). In addition, the pattern of the simulated FC matched closely with that of the empirical FC (compare Fig. 7C with 7D, and Fig. 8C with 8D). Overall, the MNMI model performed effectively in finding out the optimal parameters that generated realistic and biologically meaningful neural signals and led to simulated FC closely matched to the empirical one.

3.4. Marginal EC group differences in the default mode-salience network

The group-averaged recurrent excitation and inhibition weights within each of the seven ROIs in the DMN-SAL network are shown in Fig. 9A, B, respectively, where no significant MDD vs. NC group difference was observed. The network-averaged recurrent excitation and inhibition weights within the DMN and SAL networks are shown in Fig. 9C, D respectively. Again, there was no significant difference between the NC and MDD groups. Notably, the average recurrent excitation weight in the DMN was slightly higher than that in the SAL, while the average recurrent inhibition weight was slightly lower than that in the SAL, for both NC and MDD groups. The relatively high excitation with low inhibition may underlie the higher activation of the DMN during the resting state. The average inter-regional coupling weight within the DMN-SAL network is shown in Fig. 10. Out of the 22 estimated inter-regional weights, only the vACC → dACC connection strength was significantly decreased ($p < 0.05$, uncorrected; Cohen's d: 0.37) from -0.43 (for NC) to -0.07 (for MDD); but such a result was not significant after correction for multiple comparisons (which may only indicate marginal difference). To ensure that the lack of significant results was not due to removal of certain inter-regional connections, we applied the MNMI approach to the full DMN-SAL network and estimated all 42 inter-regional EC links (i.e., not conducting the SC-based pre-selection but excluding diagonal connections) with results shown in Supplemental Fig. S3 (no significant difference in any local connection weight) and Supplemental Fig. S4 (no significant difference in any inter-regional EC weight after multiple correction). Therefore, the model indicated that in the DMN-SAL network, there was no significant difference in connectivity between the NC and MDD groups.
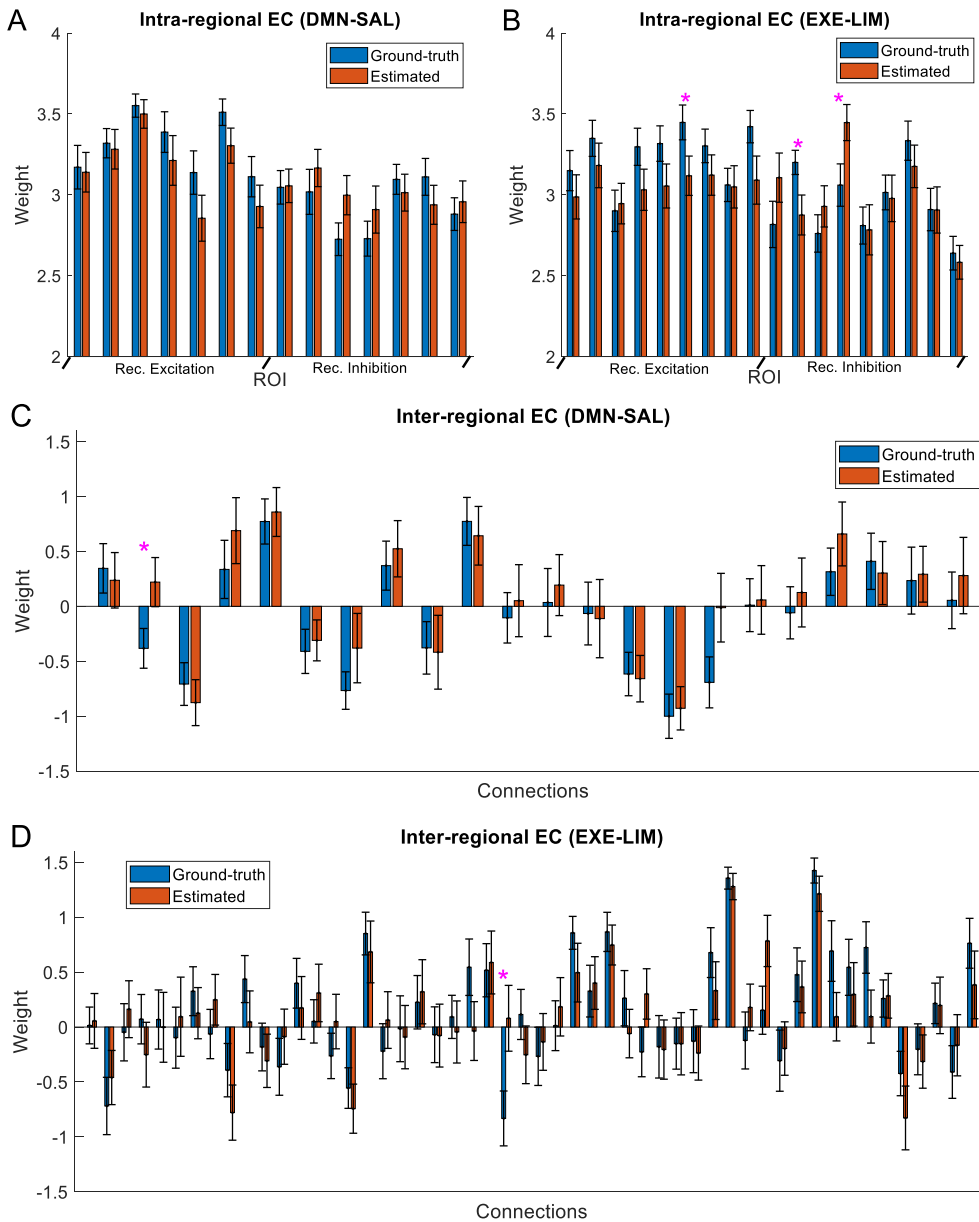
Fig. 4. Comparison between ground-truth parameters and estimated parameters in the absence of measurement noise. (A) Group-averaged intra-regional EC in the DMN-SAL network. (B) Group-averaged intra-regional EC in the EXE-LIM network. (C) Group-averaged inter-regional EC in the DMN-SAL network. (D) Group-averaged inter-regional EC in the EXE-LIM network. The pink star indicates uncorrected significant connection ($p < 0.05$, uncorrected). Error bars indicate standard error. (For interpretation of the references to colour in this figure legend, the reader is referred to the web version of this article.)

3.5. Significant EC group differences in the executive-limbic network

We next applied the MNMI approach to the EXE-LIM network, another prevalence hypothetic model, and compared both intra- and inter-regional EC between the same two groups of subjects. The group-averaged local recurrent excitation and inhibition weights and their network-specific averages are shown in Fig. 11, and the inter-regional coupling weight is shown in Fig. 12. Different from the DMN-SAL network, we observed significant difference in the intra-regional connection weight. Besides a marginal increase for the MDD in the recurrent excitation weight within the left SPC ($p < 0.05$, uncorrected; Cohen's d: 0.3; Fig. 11A), we found the recurrent inhibition weight within the left amygdala (in the limbic system) was significantly decreased in MDD ($p < 0.05$, FDR corrected; Cohen's d: −0.44; Fig. 11B). In addition, the network-averaged recurrent excitation weight within the EXE was significantly elevated in MDD ($p < 0.05$, FDR corrected; Cohen's d: 0.36; Fig. 11C), while the average recurrent inhibition weight within the LIM was significantly reduced in MDD ($p < 0.05$, FDR corrected; Cohen's d: −0.37; Fig. 11D) compared to NC.

In addition to intra-regional EC, the inter-regional EC in the EXE-LIM network also showed more significant differences in more connections between NC and MDD compared with the DMN-SAL network (Fig. 12 and Fig. 13). In particular, the within-EXE connection from the left SPC to the right dlPFC was found to switch from excitation (0.39) in NC to inhibition (-0.18) in MDD ($p < 0.05$, FDR corrected; Cohen's d: −0.51) and the EXE-to-LIM connection from the left SPC to the right amygdala was significantly increased from 0.015 in NC to 0.56 in MDD ($p < 0.05$, FDR corrected; Cohen's d: 0.47). In addition, we observed that the EXE-to-LIM connection from the left dlPFC to the left hippocampus was significantly reduced (from 0.57 to 0.039; $p < 0.05$, FDR corrected; Cohen's d: −0.46) and its mirrored connection on the other hemisphere (from the right dlPFC to the right hippocampus) was marginally decreased (from 0.73 to 0.33; $p < 0.05$, uncorrected; Cohen's d: −0.38) in MDD. Moreover, the inhibitory EXE-to-LIM connection from the right SPC to the thalamus was found to be marginally reduced (from −0.47 to −0.12; $p < 0.05$, uncorrected; Cohen's d: 0.31) in MDD. Nevertheless, we did not observe any significant difference in the network-averaged connection strength (Supplemental Fig. S5).
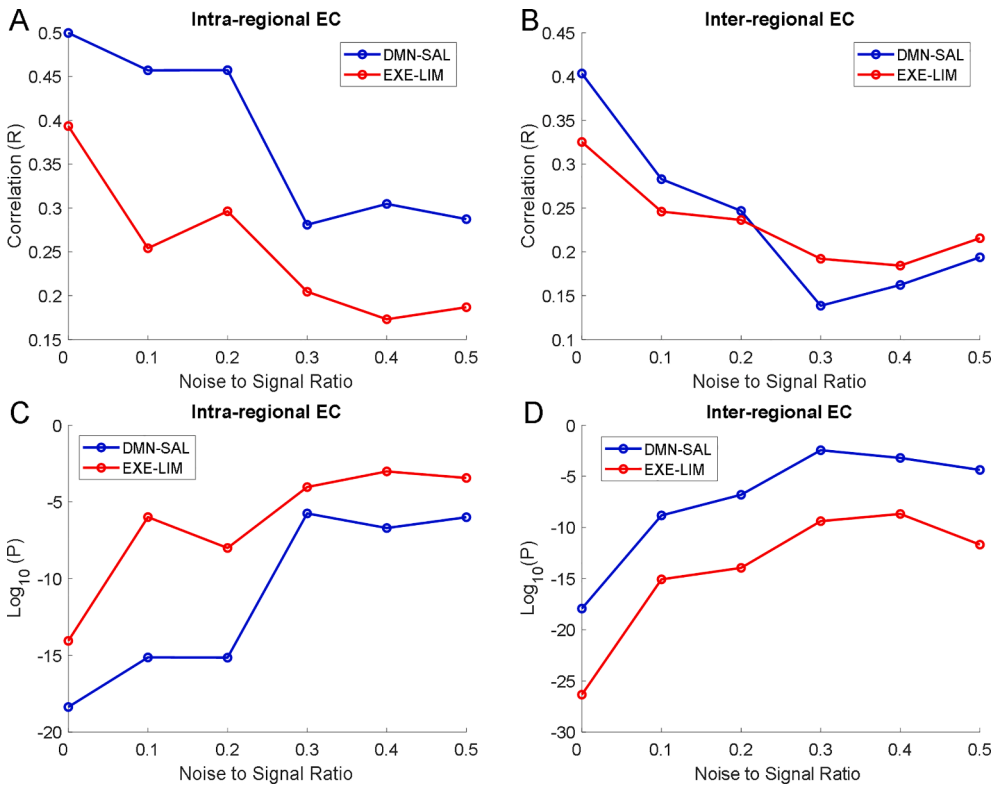
Fig. 5. Correlation between ground-truth parameters and estimated parameters as a function of noise to signal ratio. (A) Correlation coefficients of intra-regional EC. (B) Correlation coefficients of inter-regional EC. (C) P values of associative intra-regional EC correlation. (D) P values of associative inter-regional EC correlation. Correlation is calculated for all 20 synthetic subjects. Results are shown in blue for the DMN-SAL network and red for the EXE-LIM network. The P values are shown in log scale. (For interpretation of the references to colour in this figure legend, the reader is referred to the web version of this article.)
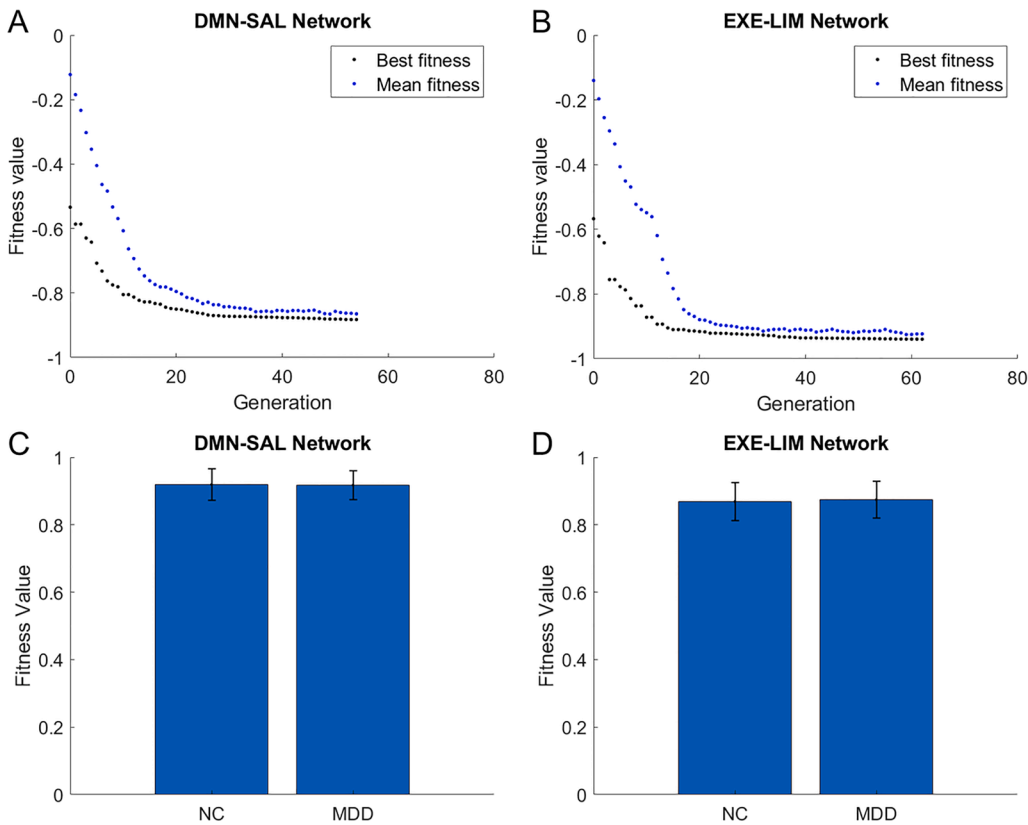

Fig. 6. Convergence of the genetic algorithm (GA). (A) Convergence of the GA for the DMN-SAL network (one subject). Blue dots: mean fitness value; black dots: best fitness value. (B) Convergence of the GA for the EXE-LIM network (one subject). (C) Average fitness value for the DMN-SAL network. (D) Average fitness value for the EXE-LIM network. Error bars indicate standard deviation. (For interpretation of the references to colour in this figure legend, the reader is referred to the web version of this article.)

3.6. A hypothetical model of executive-limbic malfunction in MDD

Based on the findings, we hypothesize that the executive-limbic network plays a central role in MDD pathophysiology and we thus propose a hypothetical model that potentially explains the disrupted cortical-limbic interactions and dynamics leading to depressive
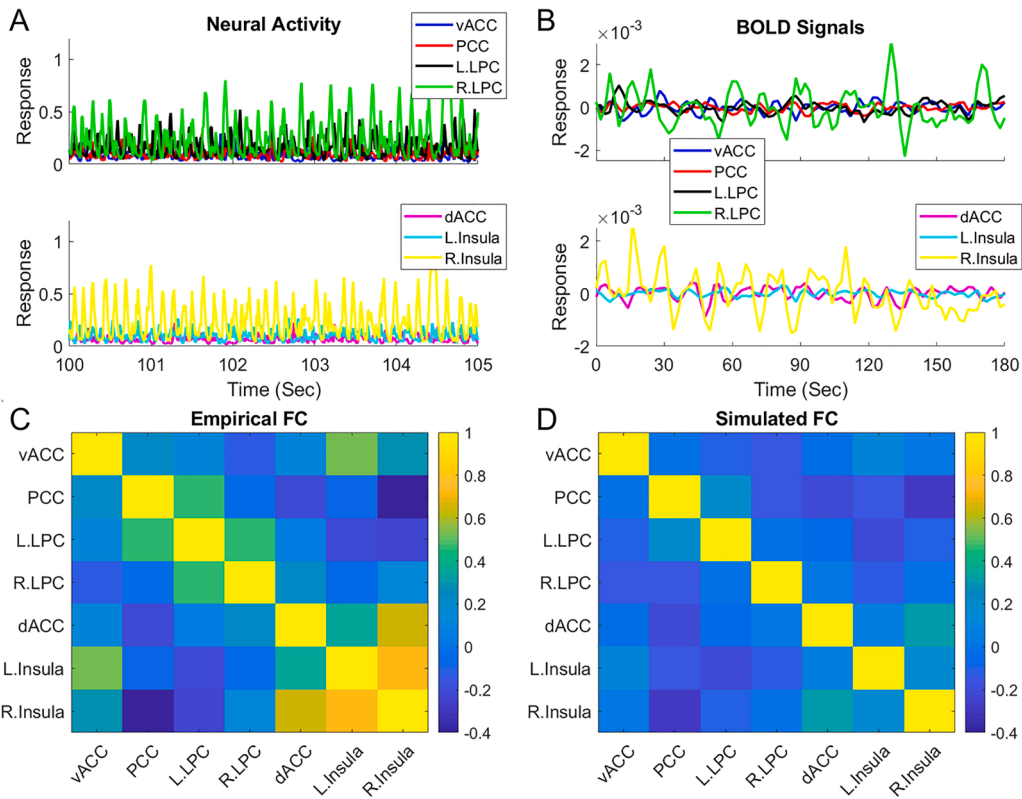
Fig. 7. Simulated output of the DMN-SAL network for one representative subject. (A) A segment of simulated activity of the excitatory neural populations from the seven ROIs. (B) Simulated BOLD signals from the seven ROIs (mean removed). (C) Empirical functional connectivity. (D) Simulated functional connectivity.
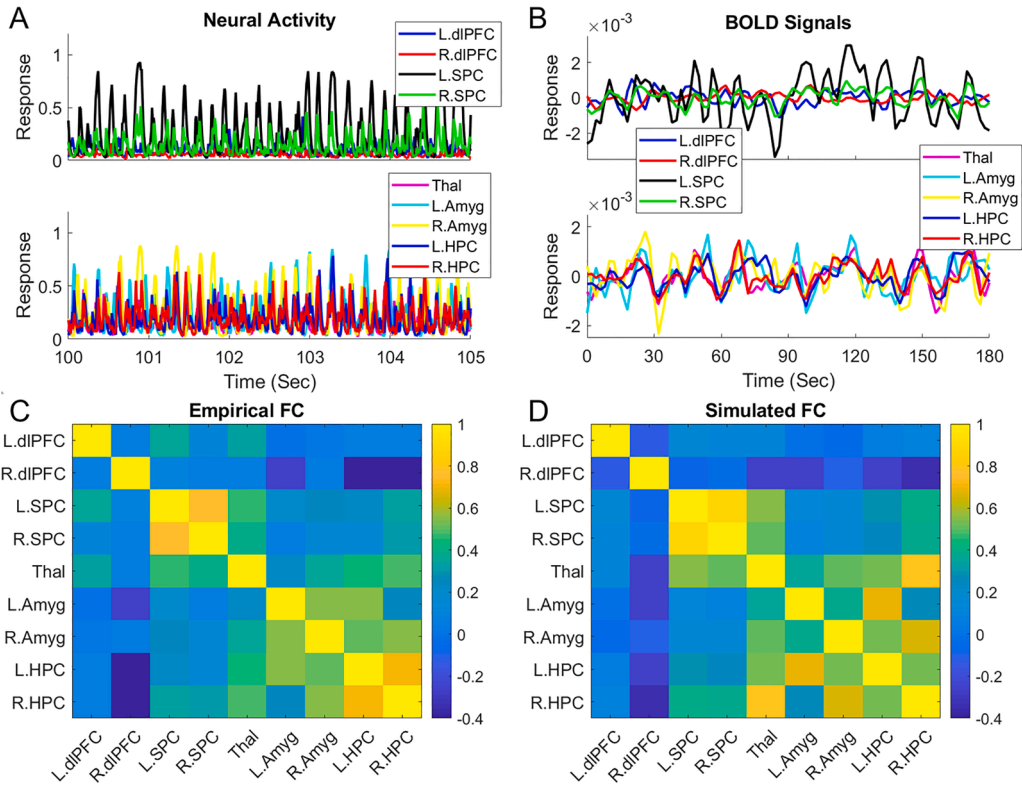

Fig. 8. Simulated output of the EXE-LIM network for one representative subject. (A) A segment of simulated activity of the excitatory neural populations from the nine ROIs. (B) Simulated BOLD signals from the nine ROIs (mean removed). (C) Empirical functional connectivity. (D) Simulated functional connectivity.
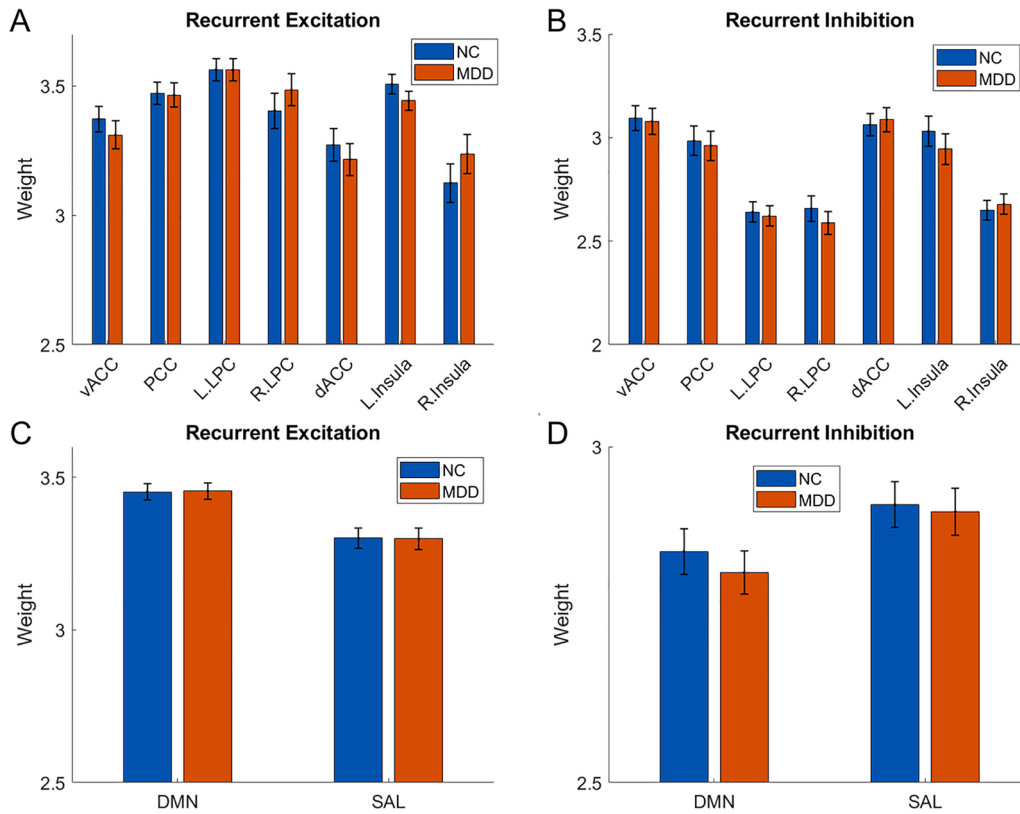
Fig. 9. Average recurrent excitation and inhibition weights between NC and MDD populations in the DMN-SAL network. (A) Average recurrent excitation weight within each ROI. (B) Average recurrent inhibition weight within each ROI. (C) Average recurrent excitation weight within the DMN and SAL networks. (D) Average recurrent inhibition weight within the DMN and SAL networks. Error bars indicate standard error.
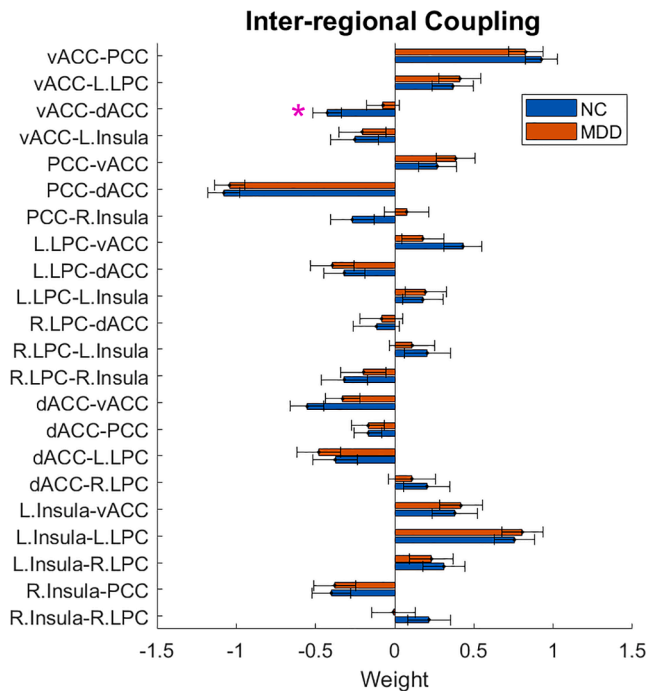

Fig. 10. Average inter-regional EC between NC and MDD populations in the DMN-SAL network. The pink star indicates uncorrected significant connection ($p < 0.05$, uncorrected). Error bars indicate standard error. (For interpretation of the references to colour in this figure legend, the reader is referred to the web version of this article.)

symptoms (Fig. 14). According to this model, the recurrent excitation within the left SPC (in EXE) is substantially increased while the recurrent inhibition within the left amygdala (in LIM) is greatly reduced in MDD, which could lead to over-excitation of these two brain regions. In the meantime, the EC from the left SPC to the right dlPFC switches from excitation in NC to inhibition in MDD, which might lead to diminished response in the right dlPFC. The SPC is involved in attending to perceptual cues in the environment (Vincent et al., 2008) and the dlPFC plays a pivotal role in attentional control and executive functioning (Elliott, 2003; Wang et al., 2018). Disrupted SPC and dlPFC activity may underlie biased attention for negative stimuli and impaired cognitive regulation of emotional processing in MDD (Fales et al., 2008; Beevers et al., 2010; Disner et al., 2011). In addition, as the EC from the right dlPFC to the right amygdala is inhibitory for both NC and MDD (Fig. 13A, B), the reduced right dlPFC response will decrease the inhibition on the right amygdala. Such a reduced inhibition, together with the significantly increased excitation from the left SPC (due to increased left SPC activity and elevated L.SPC → R.Amygdala connection strength), finally lead to overly elevated response of the right amygdala in MDD (Fig. 14). Because of the critical role of the amygdala in emotional processing and fear expression (LeDoux, 2000), excessive amygdala responses might result in depressive symptoms including increased anxiety and cognitive bias over negative stimuli (Disner et al., 2011). In another pathway, the excitatory EC from the dlPFC (in EXE) to the hippocampus (in LIM) is significantly reduced in MDD, which could in turn decrease the hippocampal responses. Due to the important role of the hippocampus in memory function (Tulving and Markowitsch, 1998), reduced hippocampal excitation may be responsible for memory impairments (Hammar and Ardal, 2009) and biased memory for negative stimuli in MDD (Disner et al., 2011). The impaired EXE-to-LIM connection also manifests as the decreased inhibition from the right SPC to the thalamus, which could in turn result in over-excitation of the
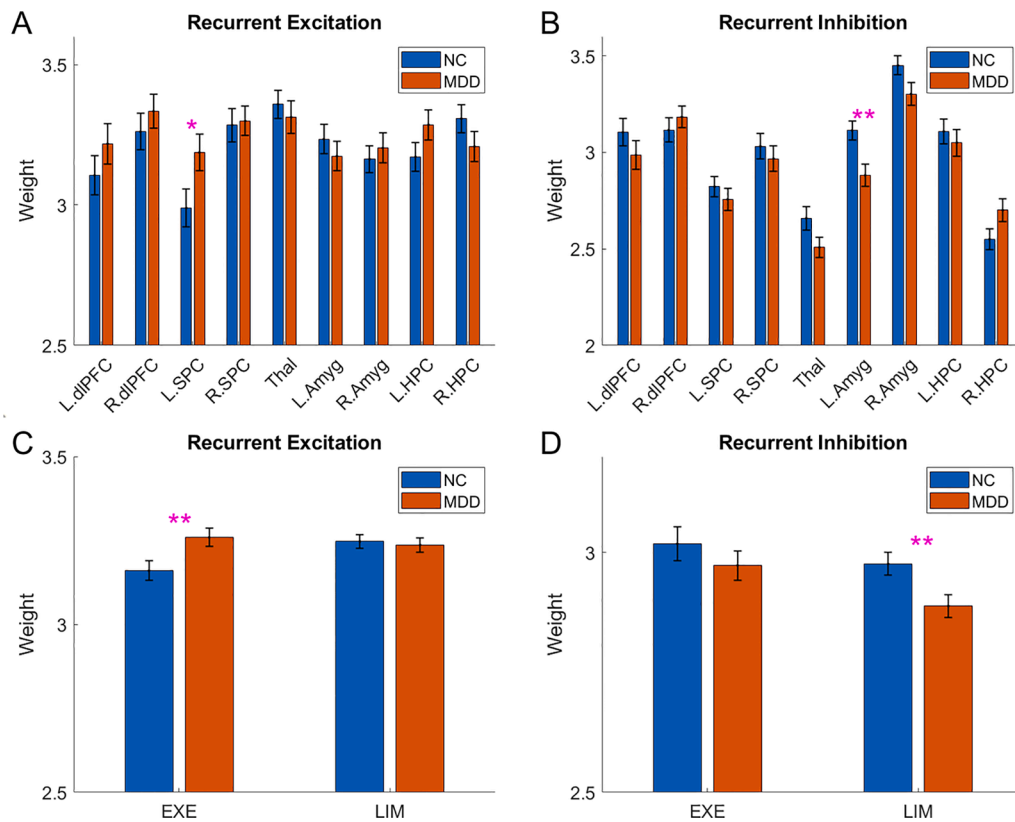
Fig. 11. Average recurrent excitation and inhibition weights between NC and MDD populations in the EXE-LIM network. (A) Average recurrent excitation weight within each ROI. (B) Average recurrent inhibition weight within each ROI. (C) Average recurrent excitation weight within the EXE and LIM networks. (D) Average recurrent inhibition weight within the EXE and LIM networks. One pink star indicates uncorrected significant connection ($p < 0.05$, uncorrected), and double pink stars indicate corrected significant connection ($p < 0.05$, corrected by FDR). Error bars indicate standard error. (For interpretation of the references to colour in this figure legend, the reader is referred to the web version of this article.)

thalamus. As the thalamus plays a central role in thalamocortical oscillations (Huguenard and McCormick, 2007; Li et al., 2017), increased thalamic excitation may lead to impaired thalamocortical rhythms through its widespread projection to the neocortex, as observed in MDD patients (Llinas et al., 1999; Hughes and Crunelli, 2005). Since thalamocortical oscillations are associated with important brain functions including arousal, attention and sensory processing (Steriade et al., 1993; Buzsaki and Draguhn, 2004; Timofeev and Bazhenov, 2005), disrupted thalamocortical rhythms may lead to insomnia, anhedonia and impaired cognitive functions in MDD.

4. Discussion

Major depressive disorder (MDD) is a complex mental disorder involving impairments in multiple large-scale brain networks and circuits (Drevets et al., 2008; Price and Drevets, 2010; Pandya et al., 2012; Drysdale et al., 2017). To achieve mechanistic understanding of this devastating disease, it is important to identify which functional networks play a central role and which functional networks play a subordinate role in the pathophysiology of MDD. Revealing the relative important role of different networks in MDD also helps to develop more effective treatments to specifically target the pathological focus for maximal therapeutic benefit. However, existing analytic approaches in fMRI focus primarily on macroscopic connectome modeling such as undirected FC and graph theory, which cannot provide a mechanistic account of circuity dysfunction. To overcome this limitation, we significantly refined a newly developed Multiscale Neural Model Inversion (MNMI) framework and applied it to test two competing hypotheses of MDD pathology (default mode – salience network disruption vs. executive – limbic network malfunction). We demonstrated that MDD is more likely caused by disrupted interaction and dynamics in a core "executive-limbic" network rather than "default mode-salience" network, consistent with the limbic-cortical dysregulation model (Mayberg, 1997, 2002; Davidson et al., 2002; Disner et al., 2011). Our

improved MNMI approach went one step further to reveal detailed underlying mechanisms of executive-limbic dysregulation at the cellular and circuit levels.

4.1. fMRI-based connectome modeling

There exist two major approaches in fMRI-based connectome modeling. The first one is statistical approach including static/dynamic FC, independent component analysis (ICA), *k*-means and hidden Markov models (Li et al., 2009b; Sporns, 2014; Preti et al., 2017). Despite the great success of these statistical techniques in characterizing the complex organizational topology of large-scale functional brain networks, their clinical translation and application to fundamental neuroscience problems are still limited in that such macroscopic network analysis is largely descriptive and superficial (Stephan et al., 2015; Braun et al., 2018). The second approach is generative modeling which relies on mechanistically or biophysically plausible neural models to simulate fMRI data and estimate model parameters using optimization algorithms (i.e., model inversion) (Friston et al., 2003; Friston, 2011). Compared to statistical approaches, generative modeling has the advantage of connecting microscale neuronal or circuit properties with macroscale network dynamics thus enabling mechanistic neuronal account of fMRI connectome. Notably, generative modeling has been widely used to infer effective connectivity (EC) among different neural populations based on fMRI (Friston et al., 2003, 2014, 2019; Gilson et al., 2016; Demirtaş et al., 2017).

Two classes of generative models have been proved to be particularly useful in studying fMRI connectome: biophysical network models (BNMs) and dynamic causal models (DCMs). BNMs of fMRI typically represent each network node with a neural mass or mean-field model of local neuronal populations and different nodes are connected via long-range fibers estimated from diffusion imaging data; the resulting network activity is then fed into a measurement model to predict fMRI signal (Honey et al., 2007; Deco and Jirsa, 2012; Deco et al., 2013b).
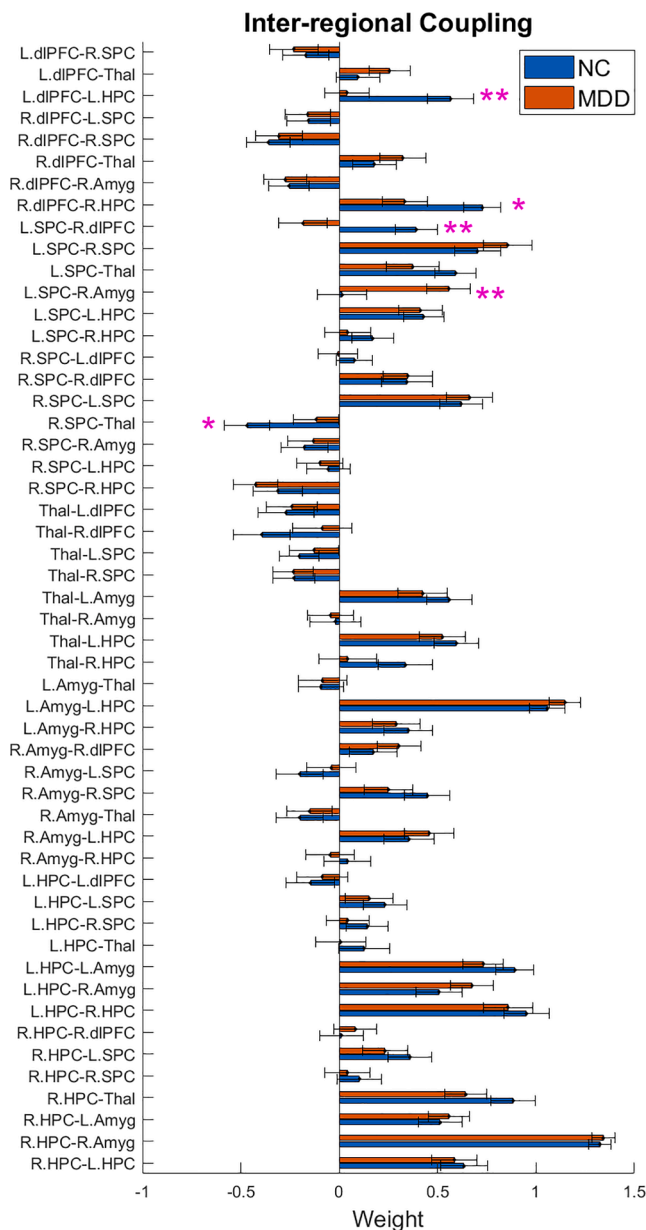
Fig. 12. Average inter-regional EC between NC and MDD populations in the EXE-LIM network. One pink star indicates uncorrected significant connection ($p < 0.05$, uncorrected), and double pink stars indicate corrected significant connection ($p < 0.05$, corrected by FDR). Error bars indicate standard error. (For interpretation of the references to colour in this figure legend, the reader is referred to the web version of this article.)

started to overcome such limitations. Using multivariate Ornstein-Uhlenbeck (MOU) process, Gilson et al. (2016, 2018, 2020) have developed BNM models that permit the inference of individual inter-regional connection strengths in large-scale networks, though intra-regional circuit interactions are not estimated.

While BNMs typically focus on simulating fMRI data, DCMs are specifically designed to infer individual connection strength at single subject level (Friston et al., 2003, 2014). Built on the Bayesian framework, DCM estimates model parameters and their marginal likelihood for both specific connections (Daunizeau et al., 2011) and network architecture (Penny et al., 2004). While DCM of electrophysiological data has incorporated biologically plausible neural mass models (NMM) to address physiological questions related to human cognition (Moran et al., 2011), attention (Auksztulewicz and Friston, 2015), and cortical hierarchies (Bastos et al., 2015), DCM for fMRI has primarily relied on a simplified bilinear state-space model (Friston et al., 2003), though two variations of DCM (stochastic DCM and spectral DCM) have been developed to specifically work with rs-fMRI (Li et al., 2011a; Friston et al., 2014). To account for intrinsic (within region) connectivity, earlier DCM used a simple two-state model including one excitatory and one inhibitory neural populations, extended from the one-state model, for each brain region (Marreiros et al., 2008). Nevertheless, the two-state model is still inherently linear, which may not capture the long-term pattern of brain spatio-temporal dynamics (Singh et al. 2020). It was not until recently the latest DCM for fMRI incorporated a more sophisticated, hierarchical convolution NMM (Friston et al., 2019). In this new version of DCM for fMRI, each brain region contains four neuronal populations and each population is represented with two implicit hidden states; the four populations are coupled with intrinsic connections modeling the inter- and intralaminar connectivity in cortical microcircuitry. The incorporation of sophisticated NMM enables DCM to explore more physiologically informed questions (Friston et al., 2019) and represents a convergence between DCMs and BNMs (Stephan et al., 2015). Of note, both the two-state DCM and NMM-based DCM currently apply to task-based fMRI only, though such limitation can be circumvented by using Fourier series as driving inputs to the models, as done previously (Di and Biswal, 2014).

Our proposed MNMI model attempts to combine the advantages of BNMs with DCMs to estimate both intra-regional and inter-regional connectivity for each individual connection and individual subject based on rs-fMRI, in a similar spirit as the latest NMM-based DCM (Friston et al., 2019). The MNMI framework differs from the two-state or NMM-based DCMs in several aspects including using the well-established Wilson-Cowan oscillator (Sejnowski, 1976; Amit and Brunel, 1997; Destexhe and Sejnowski, 2009) and a more general network architecture (instead of cortical microcircuitry) to model intrinsic neural dynamics, utilizing structural connectivity to prune inter-regional connections, fitting parameters to FC matrix instead of fMRI time series, and using GA to estimate model parameters (instead of variational Bayesian scheme; Friston et al., 2007). Of note, GA does not require prior EC expectation and allows easy computing parallelization when implemented using the MATLAB global optimization toolbox. Also, our framework is highly flexible and can be easily customized. One may choose any specific type of NMM, network architecture, objective function, and free parameters to estimate depending on the problem of interest. As an effort to bridge BNM with DCM, Singh et al. (2020) invented a new modeling framework termed Mesoscale Individualized Neurodynamic (MINDy) modeling, which fits nonlinear dynamical systems models directly to individual-level rs-fMRI data in a highly efficient matter (inversion of a large-scale model with hundreds of nodes in a few minutes). One major difference between MNMI and MINDy is that the former includes a more biologically informed NMM with excitatory/inhibitory interactions, while MINDy employs a single neural population at each node. Other differences lie in the model timescale (population firing scale vs. fMRI scale), utilization of structural information (with structural constraint vs. no structural constraint), and the specific

While BNMs have the advantage of linking population firing rates with BOLD dynamics at high spatial and temporal resolution, their ability to estimate full-scale model parameters is limited in term of individual-level data due to model complexity (Stephan et al., 2015; Singh et al., 2020). Common practices include using structural connectivity as a proxy for synaptic efficiency (Honey et al., 2007; Deco et al., 2013a; Jirsa et al., 2017), estimating a single scaling parameter for all inter-regional connections (Deco et al., 2013b; Wang et al., 2019), or estimating a small subset of parameters typically at the group-average level (Deco et al., 2014a, 2014b; Demirtaş et al., 2019). As structural connectivity is symmetric and undirected, and the use of a global scaling factor precludes the detection of selective changes at individual connections, BNMs may not accurately predict raw fMRI time series (Singh et al., 2020). It should be noted that recent advances in BNMs have
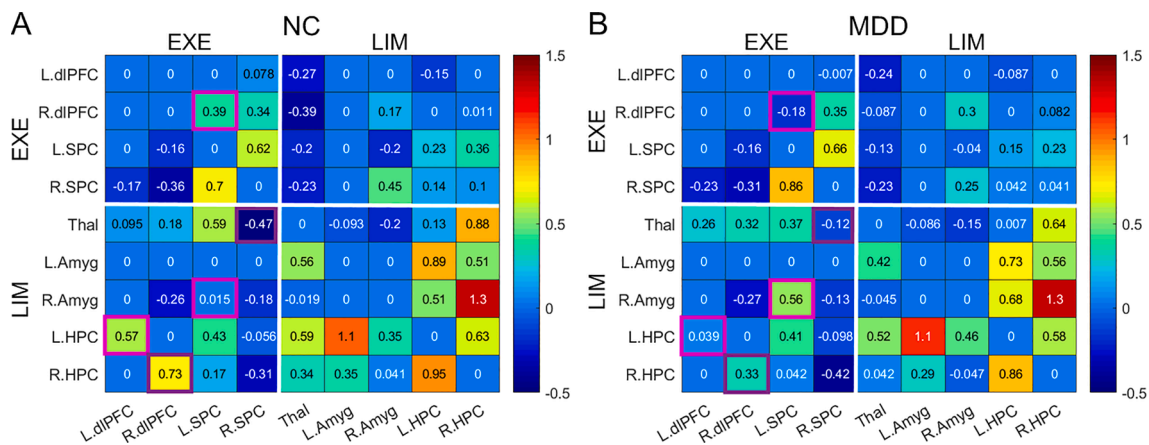
Fig. 13. Connectivity matrices within the EXE-LIM network for NC and MDD groups. (A) Average inter-regional EC for the NC group. (B) Average inter-regional EC for the MDD group. The links with significant group difference are highlighted in pink ($p < 0.05$, FDR corrected) and purple ($p < 0.05$, uncorrected) boxes. (For interpretation of the references to colour in this figure legend, the reader is referred to the web version of this article.)
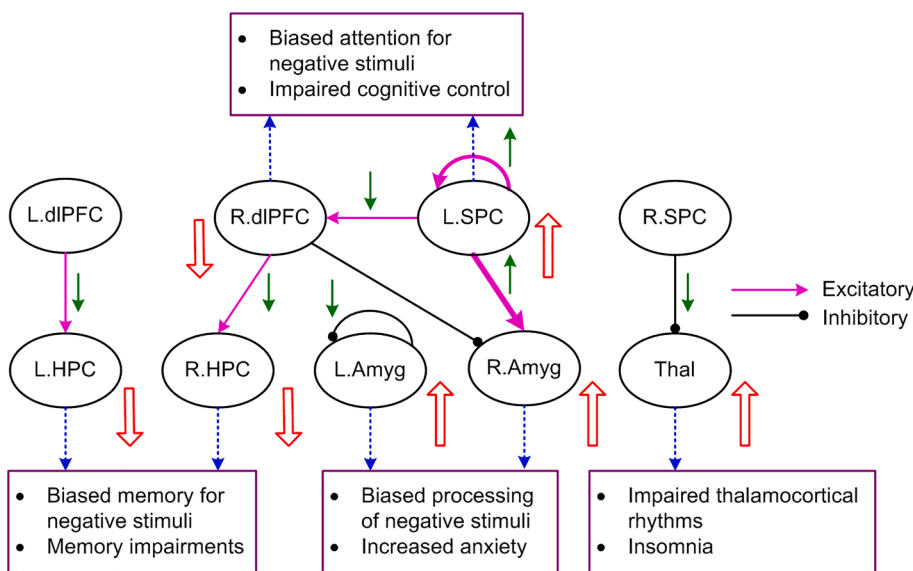

Fig. 14. A hypothetical model of executive-limbic malfunction in MDD. MDD is mediated by increased recurrent excitation in the left superior parietal cortex (L.SPC) and reduced excitation (or increased inhibition) from the L.SPC to the right dorsolateral prefrontal cortex (R.dlPFC), leading to increased response of L.SPC and decreased response of R.dlPFC, which underlie biased attention for negative stimuli and impaired cognitive control function. Also, the recurrent inhibition within the left amygdala (L.Amyg) is deceased while the excitatory drive from the L.SPC to the right amygdala (R.Amyg) is significantly increased, resulting in amygdala hyperactivity that causes biased processing of negative stimuli and increased anxiety. In addition, the excitatory projection from the left/right dlPFC to the left/right hippocampus (HPC) is abnormally decreased, leading to reduced activity of the HPC underlying biased memory for negative stimuli and other memory impairments. Moreover, the inhibition from the R.SPC to the thalamus (Thal) is reduced, which results in thalamic hyperactivity responsible for abnormal thalamocortical rhythms and insomnia. The green arrows indicate the change of the effective connectivity in MDD from normal control. The UP/DOWN arrows next to the brain regions indicate the change in neural responses in MDD compared to NC. (For interpretation of the references to colour in this figure legend, the reader is referred to the web version of this article.)

optimization scheme and algorithm (GA vs. gradient descent).

4.2. Executive-limbic malfunction as a core mechanism of MDD

One of the major finding of this study is that we identified executive-limbic malfunction as a core pathophysiological mechanism of MDD. It has long been suggested that limbic-cortical dysregulation mediates the pathogenesis of MDD (Mayberg, 1997, 2002, 2003; Davidson et al., 2002; Disner et al., 2011). However, for human MDD, it is unclear whether the dysregulation originates from limbic or cortical system and whether such dysregulation results from intrinsic (intra-regional) or inter-regional interactions. Our results demonstrate that both limbic and cortical systems and both intra-regional and inter-regional connectivities could play a role. *First*, we demonstrated that multiple intra-regional and inter-regional mechanisms underlie disrupted prefrontal-amygdala connectivity balance. Impaired prefrontal-amygdala interaction is a key component of the limbic-cortical dysregulation model (Price and Drevets, 2010; Disner et al., 2011) and an inverse relationship between amygdala and dlPFC activation has been observed (Fales et al.,

2008), suggesting the existence of an inhibitory pathway from dlPFC to downregulate amygdala. Consistently, the model reveals an inhibitory EC from the right dlPFC to the right amygdala, for both NC and MDD (Fig. 13A, B). Also, the model suggests a critical role of the SPC in dlPFC hypoactivity and amygdala hyperactivity, and SPC affects dlPFC and amygdala activity through both intrinsic and external mechanisms. On one hand, the recurrent excitation within the left SPC is marginally increased in MDD, potentially leading to increased activity of this brain region. On the other hand, the EC from the left SPC to the right dlPFC switches from excitation in NC to inhibition in MDD and the excitatory EC from the left SPC to the right amygdala greatly increases, which may account for over-inhibition of the right dlPFC and over-excitation of the right amygdala (Fig. 14). Reduced activity of the right dlPFC would decrease inhibition on the right amygdala, further contributing to amygdala hyperactivity. It should be noted that the absolute EC from the left SPC to the right dlPFC is reduced in MDD (from 0.39 to −0.18; Fig. 13A, B), consistent with decreased frontoparietal connectivity in MDD revealed by a large-scale *meta*-analysis of resting-state FC (Kaiser et al., 2015). Moreover, the model indicates a critical role of intrinsic

inhibition in amygdala hyperactivity, manifested by significantly reduced recurrent inhibition within the left amygdala (Fig. 11B). The amygdala is a heterogeneous structure consisting of multiple nucleus with excitatory and inhibitory intrinsic connections (Maren, 2001; Paré et al., 2004). The abnormally reduced recurrent inhibition within the left amygdala is consistent with the essential role of intrinsic inhibition in regulating amygdala activation and fear expression (Li et al., 2009a, 2011b).

Second, the model reveals disrupted prefrontal-hippocampus EC as an important contributor of executive-limbic malfunction. We observed that the excitatory projection from the dlPFC to the hippocampus is significantly reduced in MDD (Fig. 13), potentially resulting in reduced activity of the hippocampus. This is in agreement with decreased hippocampal volume that has been consistently found in MDD (Otte et al., 2016), possibly because the prolonged stress leads to overall neuronal atrophy and synaptic depression in the hippocampus (Chaudhury et al., 2015; Thompson et al., 2015). The potentially reduced hippocampal excitation in MDD could be in opposite to the hyperactive amygdala. Such differential excitation/inhibition modulation agrees well with the experimental observations that unlike the hippocampus, the amygdala displays increases in volume in MDD (Frodl et al., 2003) as chronic stress could induce dendritic hypertrophy (Vyas et al., 2002).

Lastly, the model indicates impaired SPC-thalamus EC in the EXE-LIM network. The thalamus is highly implicated in the MDD pathology (Drevets et al., 2008; Price and Drevets, 2010) and one previous study showed impaired PFC-thalamus FC as a key feature of treatment-resistant depression (Li et al., 2013). We found that the inhibitory EC from the right SPC to the thalamus was marginally reduced in MDD, which could potentially lead to elevated activity of the thalamus. Such a finding agrees with the experimental observation that during MDD, or the depressed phase of bipolar disorder, the glucose metabolism in the medial thalamus is abnormally increased (Price and Drevets, 2010). Thus, it is possible that the abnormal SPC-thalamus FC already exists in early depression episode, which gives way to more significant PFC-thalamus disconnectivity in the more serious, treatment-resistant depression.

4.3. Role of the default mode and salience networks in MDD

As mentioned earlier, many neuroimaging studies implicate the default mode and salience networks in the pathophysiology of MDD (Menon, 2011; Dutta et al., 2014; Mulders et al., 2015). Disrupted FC within the DMN has been frequently associated with excessive rumination and self-referential processing in MDD (Cooney et al., 2010; Hamilton et al., 2015). However, in contrast to the EXE-LIM network, the DMN-SAL network only shows marginal difference in one inter-regional EC link (Fig. 10). The marginal difference in EC is not likely due to the excessive removal of weak connections because only two inter-regional connections display marginal significance in the network without removal of weak connections (Supplemental Fig. S4). Our findings suggest that the DMN-SAL network may not be the core neural system underlying the pathogenesis of MDD. Instead, we think that they could rather constitute a secondary system whose dysfunction originates from the EXE-LIM network (and then further induces FC or EC abnormalities in the DMN and SAL). Indeed, in an integrated cognitive-biological model of MDD, it is proposed that excessive ruminative thoughts and sustained self-referential processing associated with the DMN is facilitated by heightened emotional processing from the amygdala and sustained by attenuated top-down inhibition from the dlPFC and ventrolateral PFC (Disner et al., 2011). Subsequent disrupted connectivity in the DMN may become more stable as the disease progresses, as a recent large-cohort *meta*-analysis study reported reduced FC in the DMN only in recurrent MDD, but not in FEDN (Yan et al., 2019).

On the surface, our results may be at odd with our previous study which shows that MDD is mainly associated with abnormal EC within the DMN and between the DMN and SAL networks (Li et al., 2020). Two main factors may account for such discrepancies. First, the analysis approach is different. In the previous study, we used spectral DCM (Friston et al., 2014) to estimate inter-regional EC among the DMN, EXE, SAL and LIM networks, while in the current study, we used the MNMI framework to evaluate both intra- and inter-regional EC within the DMN-SAL network and the EXE-LIM network separately. The underlying neural model of spectral DCM is essentially a linear state-space model and it estimates inter-regional EC in the *frequency* domain (Friston et al., 2014). By comparison, the MNMI method uses the more biologically realistic neural mass model and estimates both intra-regional and inter-regional EC in the *time* domain. The increased biological realism may enable us to reveal more fundamental neurophysiological mechanisms of depression. Second, as mentioned above, dysfunctional connectivity within the DMN-SAL network may be caused by executive-limbic malfunction. When the DMN-SAL network is isolated from the EXE-LIM network, most of the abnormal connectivity patterns within the DMN-SAL network may disappear. It should be noted that in Li et al. (2020), we did observe substantial abnormal EC links involving the executive and limbic networks using the parametric empirical Bayes (PEB) approach (Fig. 5b of Li et al., 2020).

4.4. Clinical implication to MDD treatment

Our findings indicate executive-limbic malfunction as a core mechanism of MDD pathophysiology. Specifically, the model predicts elevated neural activity in the superior parietal cortex, amygdala, and thalamus, along with reduced neural activity in the dlPFC and hippocampus. Based on such a hypothetic mechanism, effective treatments can be proposed to restore normal activity patterns in these brain regions to alleviate depressive symptoms. Indeed, repetitive transcranial magnetic stimulation (rTMS), an effective therapeutic modality for MDD, predominantly targets the dlPFC (Leuchter et al., 2013). The stimulation presumably increases dlPFC's excitability with concomitant downstream effects on the limbic system (Li et al., 2004; Fox et al., 2012). According to our model, boosted dlPFC activity would impose stronger inhibition on the amygdala, reducing biased processing of emotional stimuli. Besides, deep brain stimulation (DBS) of the inferior thalamic peduncle (ITP) has been shown to be effective to treatment-resistant MDD (Raymaekers et al., 2017; Dandekar et al., 2018). The ITP is a bundle of fibers that reciprocally interconnect with the thalamic reticular nucleus (TRN; Drobisz and Damborská, 2019), a subcortical structure that exerts strong inhibition on the dorsal thalamic nuclei (Pinault, 2004). Thus, stimulation of the ITP most likely reduces thalamic excitability via the TRN inhibition, which is well aligned with our model. Our model also suggests that stimulation that can dampen amygdala and superior parietal cortex activity while enhancing hippocampus excitability may have therapeutic benefit for MDD.

4.5. Model limitations

There are a few limitations associated with the present study. One major limitation is the relatively small network sizes (7 and 9 ROIs) relative to the parcellation atlas (more than 100 regions). We chose small networks as we want to focus on the core regions implicated in MDD (see Introduction). Technical considerations of MNMI (computational burden and potential over-fitting) also prevent a large-scale network inversion at present. Despite this concern, modeling a subgraph of a larger distributed network is justified provided the subgraph contains the Markov blanket of the regions in interest. Practically, this implies that the influences from outside the subgraph (i.e., other brain regions) need to be modeled with experimental inputs or endogenous fluctuations, which is naturally furnished by MNMI as every node is endowed with endogenous fluctuations. Future extension of MNMI would allow for inversion of a much larger circuit model to study MDD. A second limitation concerns the separate estimation of the DMN-SAL network and EXE-LIM network. Though we could potentially estimate

a full network model with all regions in interest and make inference on the functional roles of subnetworks, we elected to estimate the DMN-SAL and EXE-LIM networks separately because we wanted to specifically test the default mode – salience network disruption versus the executive – limbic network malfunction hypotheses. If we combine both systems together, we may not be able to disentangle which system is the cause of pathology and which system is the consequence of pathology (as disrupted activity may pass from one system to the other). Indeed, it is considered a good practice to restrict hypothesis testing or model comparison to a small number of nodes to ensure the data from the selected nodes are the most informative (Stephan et al., 2010; Daunizeau et al., 2011). Estimation of a larger network may also increase the model's susceptibility to potential over-fitting as mentioned above. It should be noted that dysconnectivity may exist among the inter-network connectivity between DMN-SAL and EXE-LIM (e.g., DMN-LIM dysconnectivity, Admon and Pizzagalli, 2015), which has not been considered by our study. Third, when using structural connectivity to constrain EC, we only considered direct (first-order) anatomical connections, while recent study has reported that indirect (high-order) anatomical connectivity can significantly sculpt EC via network diffusion (Sokolov et al., 2020). Though high-order connections were not explicitly modeled, we did observe that brain regions that are not directly coupled can still be functionally connected owing to indirect connectivity (Figs. 3, 7 and 8), which supports the role of high-order connections in EC. Lastly, for simplification, MNMI assumes fixed hemodynamic model parameters as other fMRI-based dynamic models (e.g., Frässle et al., 2017; Singh et al., 2020). This assumption is likely incorrect as interregional variability in BOLD dynamics could confound estimation of EC at the neuronal level (David et al., 2008). Future improvements of MNMI will specifically account for such regional variability by estimating hemodynamic parameters.

5. Conclusion

In conclusion, using a multiscale neural model inversion (MNMI) framework, we demonstrated that major depressive disorder is more likely characterized by disrupted circuit interactions within the executive-limbic network, rather than the default mode-salience network. We found that impaired frontoparietal effective connectivity within the executive network may contribute to hypoactivity in dlPFC, while decreased intrinsic inhibition combined with increased SPC excitation could lead to amygdala hyperactivity, together resulting in predominant PFC-amygdala activation imbalance in MDD. In addition, we observed disrupted top-down PFC-hippocampus and SPC-thalamus connectivity in MDD that could contribute to impaired memory function and abnormal thalamocortical oscillations. Our findings support the long-standing notion that limbic-cortical dysregulation underlies the pathogenesis of MDD. Future treatments should specifically target the executive-limbic system for maximal therapeutic benefits.

CRediT authorship contribution statement

Guoshi Li: Conceptualization, Methodology, Investigation, Software, Formal analysis, Visualization, Validation, Data curation, Writing - original draft, Writing - review & editing. **Yujie Liu:** Data curation, Investigation, Formal analysis. **Yanting Zheng:** Data curation, Investigation. **Ye Wu:** Formal analysis. **Danian Li:** Investigation. **Xinyu Liang:** Investigation. **Yaoping Chen:** Investigation. **Ying Cui:** Investigation. **Pew-Thian Yap:** Resources, Supervision, Funding acquisition, Writing - review & editing. **Shijun Qiu:** Investigation, Resources, Supervision, Funding acquisition. **Han Zhang:** Investigation, Supervision, Writing - review & editing. **Dinggang Shen:** Resources, Supervision, Funding acquisition, Writing - review & editing.

Declaration of Competing Interest

The authors declare that they have no known competing financial interests or personal relationships that could have appeared to influence the work reported in this paper.

Appendix A. Supplementary data

Supplementary data to this article can be found online at https://doi.org/10.1016/j.nicl.2021.102758.

References

Abeysuriya, R.G., Hadida, J., Sotiropoulos, S.N., Jbabdi, S., Becker, R., Hunt, B.A.E., Brookes, M.J., Woolrich, M.W., Marinazzo, D., 2018. A biophysical model of dynamic balancing of excitation and inhibition in fast oscillatory large-scale networks. PLoS Comput. Biol. 14 (2), e1006007.

Admon, R., Pizzagalli, D., 2015. Corticostriatal pathways contribute to the natural time course of positive mood. Nat. Commun. 6, 10065.

Almeida, J.R.C., Kronhaus, D.M., Sibille, E.L., Langenecker, S.A., Versace, A., Labarbara, E.J., Phillips, M.L., 2011. Abnormal left-sided orbitomedial prefrontal cortical-amygdala connectivity during happy and fear face processing: a potential neural mechanism of female MDD. Front. Psychiatry 2, 69.

Almeida, J.R.C., Versace, A., Mechelli, A., Hassel, S., Quevedo, K., Kupfer, D.J., Phillips, M.L., 2009. Abnormal amygdala-prefrontal effective connectivity to happy faces differentiates bipolar from major depression. Biol. Psychiatry 66 (5), 451–459.

American Psychiatric Association, 2013. Diagnostic and statistical manual of mental disorders: DSM-5, 5th ed. American Psychiatric Publishing Inc., Arlington, VA, US.

Amit, D.J., Brunel, N., 1997. Model of global spontaneous activity and local structured activity during delay periods in the cerebral cortex. Cereb. Cortex 7, 237–252.

Auksztulewicz, R., Friston, K., 2015. Attentional enhancement of auditory mismatch responses: a DCM/MEG study. Cereb. Cortex 25 (11), 4273–4283.

Avery, J.A., Drevets, W.C., Moseman, S.E., Bodurka, J., Barcalow, J.C., Simmons, W.K., 2014. Major depressive disorder is associated with abnormal interoceptiveactivity and functional connectivity in the insula. Biol. Psychiatry 76 (3), 258–266.

Balaev, V., Orlov, I., Petrushevsky, A., Martynova, O., 2018. Functional connectivity between salience, default mode and frontoparietal networks in post-stroke depression. J. Affect. Disord. 227, 554–562.

Bastos, A.M., Litvak, V., Moran, R., Bosman, C.A., Fries, P., Friston, K.J., 2015. A DCM study of spectral asymmetries in feedforward and feedback connections between visual areas V1 and V4 in the monkey. Neuroimage 108, 460–475.

Becker, R., Knock, S., Ritter, P., Jirsa, V., Daunizeau, J., 2015. Relating alpha power and phase to population firing and hemodynamic activity using a thalamo-cortical neural mass model. PLoS Comput. Biol. 11 (9), e1004352.

Beevers, C.G., Clasen, P., Stice, E., Schnyer, D., 2010. Depression symptoms and cognitive control of emotion cues: a functional magnetic resonance imaging study. Neuroscience 167 (1), 97–103.

Benjamini, Y., Yekutieli, D., 2001. The control of the false discovery rate in multiple testing under dependency. Ann. Stat. 29, 1165–1188.

Braun, U., Schaefer, A., Betzel, R.F., Tost, H., Meyer-Lindenberg, A., Bassett, D.S., 2018. From maps to multi-dimensional network mechanisms of mental disorders. Neuron 97 (1), 14–31.

Buzsaki, G., Draguhn, A., 2004. Neuronal oscillations in cortical networks. Science 304, 1926–1929.

Chaudhury, D., Liu, H.e., Han, M.-H., 2015. Neuronal correlates of depression. Cell. Mol. Life Sci. 72 (24), 4825–4848.

Cooney, R.E., Joormann, J., Eugène, F., Dennis, E.L., Gotlib, I.H., 2010. Neural correlates of rumination in depression. Cogn. Affect. Behav. Neurosci. 10 (4), 470–478.

Corbetta, M., Shulman, G.L., 2002. Control of goal-directed and stimulus-driven attention in the brain. Nat. Rev. Neurosci. 3 (3), 201–215.

Dandekar, M.P., Fenoy, A.J., Carvalho, A.F., Soares, J.C., Quevedo, J., 2018. Deep brain stimulation for treatment-resistant depression: an integrative review of preclinical and clinical findings and translational implications. Mol. Psychiatry 23 (5), 1094–1112.

Daunizeau, J., David, O., Stephan, K.E., 2011. Dynamic causal modelling: a critical review of the biophysical and statistical foundations. Neuroimage 58 (2), 312–322.

David, O., Guillemain, I., Saillet, S., Reyt, S., Deransart, C., Segebarth, C., Depaulis, A., Valdes-Sosa, P., 2008. Identifying neural drivers with functional MRI: an electrophysiological validation. PLoS Biol. 6 (12), e315.

Davidson, R.J., Pizzagalli, D., Nitschke, J.B., Putnam, K., 2002. Depression: perspectives from affective neuroscience. Annu. Rev. Psychol. 53 (1), 545–574.

Deco, G., Jirsa, V.K., 2012. Ongoing cortical activity at rest: criticality, multistability, and ghost attractors. J. Neurosci. 32 (10), 3366–3375.

Deco, G., Jirsa, V.K., McIntosh, A.R., 2013a. Resting brains never rest: computational insights into potential cognitive architectures. Trends Neurosci. 36 (5), 268–274.

Deco, G., McIntosh, A.R., Shen, K., Hutchison, R.M., Menon, R.S., Everling, S., Hagmann, P., Jirsa, V.K., 2014a. Identification of optimal structural connectivity using functional connectivity and neural modeling. J. Neurosci. 34 (23), 7910–7916.

Deco, G., Ponce-Alvarez, A., Hagmann, P., Romani, G.L., Mantini, D., Corbetta, M., 2014b. How local excitation-inhibition ratio impacts the whole brain dynamics. J. Neurosci. 34 (23), 7886–7898.

Deco, G., Ponce-Alvarez, A., Mantini, D., Romani, G.L., Hagmann, P., Corbetta, M., 2013b. Resting-state functional connectivity emerges from structurally and dynamically shaped slow linear fluctuations. J. Neurosci. 33 (27), 11239–11252.

Delaloye, S., Holtzheimer, P.E., 2014. Deep brain stimulation in the treatment of depression. Dialogues Clin. Neurosci. 16, 83–91.

Demirtaş, M., Burt, J.B., Helmer, M., Ji, J.L., Adkinson, B.D., Glasser, M.F., Van Essen, D. C., Sotiropoulos, S.N., Anticevic, A., Murray, J.D., 2019. Hierarchical heterogeneity across human cortex shapes large-scale neural dynamics. Neuron 101 (6), 1181–1194.e13.

Demirtaş, M., Falcon, C., Tucholka, A., Gispert, J.D., Molinuevo, J.L., Deco, G., 2017. A whole-brain computational modeling approach to explain the alterations in resting-state functional connectivity during progression of Alzheimer's disease. Neuroimage Clin 16, 343–354.

Destexhe, A., Sejnowski, T.J., 2009. The Wilson Cowan model, 36 years later. Biol. Cybern. 101, 1–2.

Destrieux, C., Fischl, B., Dale, A., Halgren, E., 2010. Automatic parcellation of human cortical gyri and sulci using standard anatomical nomenclature. Neuroimage 53 (1), 1–15.

Di, X., Biswal, B.B., 2014. Identifying the default mode network structure using dynamic causal modeling on resting-state functional magnetic resonance imaging. Neuroimage 86, 53–59.

Disner, S.G., Beevers, C.G., Haigh, E.A.P., Beck, A.T., 2011. Neural mechanisms of the cognitive model of depression. Nat. Rev. Neurosci. 12 (8), 467–477.

Drevets, W.C., 2001. Neuroimaging and neuropathological studies of depression: implications for the cognitive-emotional features of mood disorders. Curr. Opin. Neurobiol. 11 (2), 240–249.

Drevets, W.C., Price, J.L., Furey, M.L., 2008. Brain structural and functional abnormalities in mood disorders: implications for neurocircuitry models of depression. Brain Struct. Funct. 213 (1-2), 93–118.

Drobisz, D., Damborská, A., 2019. Deep brain stimulation targets for treating depression. Behav. Brain Res. 359, 266–273.

Drysdale, A.T., Grosenick, L., Downar, J., Dunlop, K., Mansouri, F., Meng, Y., Fetcho, R. N., Zebley, B., Oathes, D.J., Etkin, A., Schatzberg, A.F., Sudheimer, K., Keller, J., Mayberg, H.S., Gunning, F.M., Alexopoulos, G.S., Fox, M.D., Pascual-Leone, A., Voss, H.U., Casey, B.J., Dubin, M.J., Liston, C., 2017. Resting-state connectivity biomarkers define neurophysiological subtypes of depression. Nat. Med. 23 (1), 28–38.

Dutta, A., McKie, S., Deakin, J.F.W., 2014. Resting state networks in major depressive disorder. Psychiatry Res.: Neuroimaging 224 (3), 139–151.

Elliott R (2003) Executive functions and their disorders. British Med. Bull. 65, 49–59.

Fales, C.L., Barch, D.M., Rundle, M.M., Mintun, M.A., Snyder, A.Z., Cohen, J.D., Mathews, J., Sheline, Y.I., 2008. Altered emotional interference processing in affective and cognitive-control brain circuitry in major depression. Biol. Psychiatry 63 (4), 377–384.

Fox, M.D., Buckner, R.L., White, M.P., Greicius, M.D., Pascual-Leone, A., 2012. Efficacy of transcranial magnetic stimulation targets for depression is related to intrinsic functional connectivity with the subgenual cingulate. Biol. Psychiatry 72 (7), 595–603.

Frässle, S., Lomakina, E.I., Razi, A., Friston, K.J., Buhmann, J.M., Stephan, K.E., 2017. Regression DCM for fMRI. Neuroimage 155, 406–421.

Friston, K.J., 2011. Functional and effective connectivity: a review. Brain Connect. 1 (1), 13–36.

Friston, K.J., Harrison, L., Penny, W., 2003. Dynamic causal modeling. Neuroimage 19, 1273–1302.

Friston, K.J., Kahan, J., Biswal, B., Razi, A., 2014. A DCM for resting state fMRI. Neuroimage 94, 396–407.

Friston, K., Mattout, J., Trujillo-Barreto, N., Ashburner, J., Penny, W., 2007. Variational free energy and the Laplace approximation. Neuroimage 34 (1), 220–234.

Friston, K.J., Preller, K.H., Mathys, C., Cagnan, H., Heinzle, J., Razi, A., Zeidman, P., 2019. Dynamic causal modelling revisited. Neuroimage 199, 730–744.

Frodl, T., Meisenzahl, E.M., Zetzsche, T., Born, C., Jäger, M., Groll, C., Bottlender, R., Leinsinger, G., Möller, H.-J., 2003. Larger amygdala volumes in first depressive episode as compared to recurrent major depression and healthy control subjects. Biol. Psychiatry 53 (4), 338–344.

Gilson, M., Deco, G., Friston, K.J., Hagmann, P., Mantini, D., Betti, V., Romani, G.L., Corbetta, M., 2018. Effective connectivity inferred from fMRI transition dynamics during movie viewing points to a balanced reconfiguration of cortical interactions. Neuroimage 180, 534–546.

Gilson, M., Moreno-Bote, R., Ponce-Alvarez, A., Ritter, P., Deco, G., Jbabdi, S., 2016. Estimation of directed effective connectivity from fMRI functional connectivity hints at asymmetries of cortical connectome. PLoS Comput. Biol. 12 (3), e1004762.

Gilson, M., Zamora-López, G., Pallarés, V., Adhikari, M.H., Senden, M., Campo, A.T., Mantini, D., Corbetta, M., Deco, G., Insabato, A., 2020. Model-based whole-brain effective connectivity to study distributed cognition in health and disease. Network Neurosci. 4 (2), 338–373.

Gong, Q., He, Y., 2015. Depression, neuroimaging and connectomics: a selective overview. Biol. Psychiatry 77 (3), 223–235.

Hamilton, J.P., Etkin, A., Furman, D.J., Lemus, M.G., Johnson, R.F., Gotlib, I.H., 2012. Functional neuroimaging of major depressive disorder: a meta-analysis and new integration of base line activation and neural response data. Am. J. Psychiatry 169 (7), 693–703.

Hamilton, J.P., Farmer, M., Fogelman, P., Gotlib, I.H., 2015. Depressive rumination, the default-mode network, and the dark matter of clinical neuroscience. Biol. Psychiatry 78 (4), 224–230.

Hamilton M (1967) Development of a rating scale for primary depressive illness. British J. Social Clin. Psychol. 6, 278–296.

Hammar, A., Ardal, G., 2009. Cognitive functioning in major depression - a summary. Front. Hum. Neurosci. 3, 26.

Hellyer, P.J., Jachs, B., Clopath, C., Leech, R., 2016. Local inhibitory plasticity tunes macroscopic brain dynamics and allows the emergence of functional brain networks. Neuroimage 124, 85–95.

Hermans, E.J., Henckens, M.J.A.G., Joëls, M., Fernández, G., 2014. Dynamic adaptation of large-scale brain networks in response to acute stressors. Trends Neurosci. 37 (6), 304–314.

Honey, C.J., Kotter, R., Breakspear, M., Sporns, O., 2007. Network structure of cerebral cortex shapes functional connectivity on multiple time scales. PNAS 104 (24), 10240–10245.

Hughes, S.W., Crunelli, V., 2005. Thalamic mechanisms of EEG alpha rhythms and their pathological implications. Neuroscientist 11 (4), 357–372.

Huguenard, J.R., McCormick, D.A., 2007. Thalamic synchrony and dynamic regulation of global forebrain oscillations. Trends Neurosci. 30 (7), 350–356.

Hyett, M.P., Breakspear, M.J., Friston, K.J., Guo, C.C., Parker, G.B., 2015. Disrupted effective connectivity of cortical systems supporting attention and interoception in melancholia. JAMA Psychiatry 72 (4), 350.

Jirsa, V.K., Proix, T., Perdikis, D., Woodman, M.M., Wang, H., Gonzalez-Martinez, J., Bernard, C., Bénar, C., Guye, M., Chauvel, P., Bartolomei, F., 2017. The virtual epileptic patient: individualized whole-brain models of epilepsy spread. Neuroimage 145, 377–388.

Kaiser, R.H., Andrews-Hanna, J.R., Wager, T.D., Pizzagalli, D.A., 2015. Large-scale network dysfunction in major depressive disorder: a meta-analysis of resting-state functional connectivity. JAMA Psychiatry 72 (6), 603.

Kandilarova, S., Stoyanov, D., Kostianev, S., Specht, K., 2018. Altered resting state effective connectivity of anterior insula in depression. Front. Psychiatry 9, 83.

Kessler, R.C., Berglund, P., Demler, O., Jin, R., Merikangas, K.R., Walters, E.E., 2005. Lifetime prevalence and age-of-onset distributions of DSM-IV disorders in the National Comorbidity Survey Replication. Arch. Gen. Psychiatry 62 (6), 593.

Koechlin, E., Summerfield, C., 2007. An information theoretical approach to prefrontal executive function. Trends Cogn. Sci. 11 (6), 229–235.

LeDoux, J.E., 2000. Emotion circuits in the brain. Annu. Rev. Neurosci. 23 (1), 155–184.

Lener, M.S., Niciu, M.J., Ballard, E.D., Park, M., Park, L.T., Nugent, A.C., Zarate, C.A., 2017. Glutamate and gamma-aminobutyric acid systems in the pathophysiology of major depression and antidepressant response to ketamine. Biol. Psychiatry 81 (10), 886–897.

Leuchter, A.F., Cook, I.A., Jin, Y., Phillips, B., 2013. The relationship between brain oscillatory activity and therapeutic effectiveness of transcranial magnetic stimulation in the treatment of major depressive disorder. Front. Hum. Neurosci. 7, 37.

Li, B., Daunizeau, J., Stephan, K.E., Penny, W., Hu, D., Friston, K.J., 2011a. Generalised filtering and stochastic DCM for fMRI. Neuroimage 58, 442–457.

Li, C.T., Chen, L.F., Tu, P.C., Wang, S.J., Chen, M.H., Su, T.P., Hsieh, J.C., 2013. Impaired prefronto-thalamic functional connectivity as a key feature of treatment-resistant depression: a combined MEG, PET and rTMS study. PLoS One 8, e70699.

Li, G., Amano, T., Pare, D., Nair, S.S., 2011b. Impact of infralimbic inputs on intercalated amygdala neurons: A biophysical modeling study. Learning Memory 18 (4), 226–240.

Li, G., Henriquez, C.S., Fröhlich, F., Gutkin, B.S., 2017a. Unified thalamic model generates multiple distinct oscillations with state-dependent entrainment by stimulation. PLoS Comput. Biol. 13 (10), e1005797.

Li, G., Liu, Y., Zheng, Y., Li, D., Liang, X., Chen, Y., Cui, Y., Yap, P.-T., Qiu, S., Zhang, H., Shen, D., 2020. Large-scale dynamic causal modeling of major depressive disorder based on resting-state functional magnetic resonance imaging. Hum. Brain Mapp. 41 (4), 865–881.

Li, G., Liu, Y., Zheng, Y., Wu, Y., Yap, P., Qiu, S., Zhang, H., Shen, D., 2019. Identification of abnormal circuit dynamics in major depressive disorder via multiscale neural modeling of resting-state fMRI. In: Shen, D. (Ed.), Medical Image Computing and Computer Assisted Intervention – MICCAI, 11766. Springer, Cham, pp. 682–690.

Li, G., Nair, S.S., Quirk, G.J., 2009a. A biologically realistic network model of acquisition and extinction of conditioned fear associations in lateral amygdala neurons. J. Neurophysiol. 101 (3), 1629–1646.

Li, K., Guo, L., Nie, J., Li, G., Liu, T., 2009b. Review of methods for functional brain connectivity detection using fMRI. Comput. Med. Imaging Graph. 33 (2), 131–139.

Li, L., Li, B., Bai, Y., Liu, W., Wang, H., Leung, H.-C., Tian, P., Zhang, L., Guo, F., Cui, L.-B., Yin, H., Lu, H., Tan, Q., 2017b. Abnormal resting state effective connectivity

within the default mode network in major depressive disorder: a spectral dynamic causal modeling study. Brain Behav 7 (7), e00732.

Li, X., Nahas, Z., Kozel, F.A., Anderson, B., Bohning, D.E., George, M.S., 2004. Acute left prefrontal transcranial magnetic stimulation in depressed patients is associated with immediately increased activity in prefrontal cortical as well as subcortical regions. Biol. Psychiatry 55 (9), 882–890.

Liston, C., Chen, A.C., Zebley, B.D., Drysdale, A.T., Gordon, R., Leuchter, B., Voss, H.U., Casey, B.J., Etkin, A., Dubin, M.J., 2014. Default mode network mechanisms of transcranial magnetic stimulation in depression. Biol. Psychiatry 76 (7), 517–526.

Llinas, R.R., Ribary, U., Jeanmonod, D., Kronberg, E., Mitra, P.P., 1999. Thalamocortical dysrhythmia: a neurological and neuropsychiatric syndrome characterized by magnetoencephalography. PNAS 96 (26), 15222–15227.

Lu, Q., Li, H., Luo, G., Wang, Y.i., Tang, H., Han, L.i., Yao, Z., 2012. Impaired prefrontal-amygdala effective connectivity is responsible for the dysfunction of emotion process in major depressive disorder: A dynamic causal modeling study on MEG. Neurosci. Lett. 523 (2), 125–130.

Maier-Hein, K.H., Neher, P.F., Houde, J.-C., Côté, M.-A., Garyfallidis, E., Zhong, J., Chamberland, M., Yeh, F.-C., Lin, Y.-C., Ji, Q., Reddick, W.E., Glass, J.O., Chen, D.Q., Feng, Y., Gao, C., Wu, Y.e., Ma, J., He, R., Li, Q., Westin, C.-F., Deslauriers-Gauthier, S., González, J.O.O., Paquette, M., St-Jean, S., Girard, G., Rheault, F., Sidhu, J., Tax, C.M.W., Guo, F., Mesri, H.Y., Dávid, S., Froeling, M., Heemskerk, A.M., Leemans, A., Boré, A., Pinsard, B., Bedetti, C., Desrosiers, M., Brambati, S., Doyon, J., Sarica, A., Vasta, R., Cerasa, A., Quattrone, A., Yeatman, J., Khan, A.R., Hodges, W., Alexander, S., Romascano, D., Barakovic, M., Auría, A., Esteban, O., Lemkaddem, A., Thiran, J.-P., Cetingul, H.E., Odry, B.L., Mailhe, B., Nadar, M.S., Pizzagalli, F., Prasad, G., Villalon-Reina, J.E., Galvis, J., Thompson, P.M., Requejo, F. D.S., Laguna, P.L., Lacerda, L.M., Barrett, R., Dell'Acqua, F., Catani, M., Petit, L., Caruyer, E., Daducci, A., Dyrby, T.B., Holland-Letz, T., Hilgetag, C.C., Stieltjes, B., Descoteaux, M., 2017. The challenge of mapping the human connectome based on diffusion tractography. Nat. Commun. 8 (1).

Manoliu, A., Meng, C., Brandl, F., Doll, A., Tahmasian, M., Scherr, M., Schwerthöffer, D., Zimmer, C., Förstl, H., Bäuml, J., Riedl, V., Wohlschläger, A.M., Sorg, C., 2014. Insular dysfunction within the salience network is associated with severity of symptoms and aberrant inter-network connectivity in major depressive disorder. Front. Hum. Neurosci. 7, 1–17.

Maren, S., 2001. Neurobiology of Pavlovian fear conditioning. Annu. Rev. Neurosci. 24 (1), 897–931.

Marreiros, A.C., Kiebel, S.J., Friston, K.J., 2008. Dynamic causal modelling for fMRI: a two-state approach. Neuroimage 39 (1), 269–278.

Mayberg, H.S., 1997. Limbic-cortical dysregulation: a proposed model of depression. J. Neuropsychiatry Clin. Neurosci. 9, 471–481.

Mayberg, H.S., 2002. Mapping mood: an evolving emphasis on frontal–limbic interactions. In: Stuss, D.T., Knight, R.T. (Eds.), Principles of Frontal Lobe Function. Oxford University Press, Oxford, pp. 376–391.

Mayberg, H.S., 2003. Modulating dysfunctional limbic-cortical circuits in depression: towards development of brain-based algorithms for diagnosis and optimised treatment. Br. Med. Bull. 65, 193–207.

Menon, V., 2011. Large-scale brain networks and psychopathology: a unifying triple network model. Trends Cogn Sci 15 (10), 483–506.

Miller, E.K., Cohen, J.D., 2001. An integrative theory of prefrontal cortex function. Annu. Rev. Neurosci. 24 (1), 167–202.

Mitchell, M., 1995. Genetic algorithms: an overview. Complexity 1 (1), 31–39.

Moran, R.J., Symmonds, M., Stephan, K.E., Friston, K.J., Dolan, R.J., 2011. An in vivo assay of synaptic function mediating human cognition. Curr. Biol. 21, 1320–1325.

Mulders, P.C., van Eijndhoven, P.F., Schene, A.H., Beckmann, C.F., Tendolkar, I., 2015. Resting-state functional connectivity in major depressive disorder: a review. Neurosci. Biobehav. Rev. 56, 330–344.

Ochsner, K.N., Ray, R.D., Cooper, J.C., Robertson, E.R., Chopra, S., Gabrieli, J.D.E., Gross, J.J., 2004. For better or for worse: neural systems supporting the cognitive down- and up-regulation of negative emotion. Neuroimage 23 (2), 483–499.

Otte, C., Gold, S.M., Penninx, B.W., Pariante, C.M., Etkin, A., Fava, M., Mohr, D.C., Schatzberg, A.F., 2016. Major depressive disorder. Nat. Rev. Dis. Primers 2, 16065.

Pandya, M., Altinay, M., Malone, D.A., Anand, A., 2012. Where in the brain is depression? Curr. Psychiatry Rep. 14 (6), 634–642.

Paré, D., Quirk, G.J., Ledoux, J.E., 2004. New vistas on amygdala networks in conditioned fear. J. Neurophysiol. 92 (1), 1–9.

Penny, W.D., Stephan, K.E., Mechelli, A., Friston, K.J., 2004. Comparing dynamic causal models. Neuroimage 22 (3), 1157–1172.

Petrides, M., 2005. Lateral prefrontal cortex: architectonic and functional organization. Philos. Trans. R. Soc. Lond. B Biol. Sci. 360 (1456), 781–795.

Phillips, M.L., Ladouceur, C.D., Drevets, W.C., 2008. A neural model of voluntary and automatic emotion regulation: implications for understanding the pathophysiology and neurodevelopment of bipolar disorder. Mol. Psychiatry 13, 829–857.

Pinault, D., 2004. The thalamic reticular nucleus: structure, function and concept. Brain Res. Rev. 46 (1), 1–31.

Power, J.D., Barnes, K.A., Snyder, A.Z., Schlaggar, B.L., Petersen, S.E., 2012. Spurious but systematic correlations in functional connectivity MRI networks arise from subject motion. Neuroimage 59 (3), 2142–2154.

Preti, M.G., Bolton, T.AW., Van De Ville, D., 2017. The dynamic functional connectome: State-of-the-art and perspectives. Neuroimage 160, 41–54.

Price, J.L., Drevets, W.C., 2010. Neurocircuitry of mood disorders. Neuropsychopharmacology 35 (1), 192–216.

Quirk, G.J., Likhtik, E., Pelletier, J.G., Paré, D., 2003. Stimulation of medial prefrontal cortex decreases the responsiveness of central amygdala output neurons. J. Neurosci. 23 (25), 8800–8807.

Raichle, M.E., 2011. The restless brain. Brain Connect. 1, 3–12.

Ray, R.D., Ochsner, K.N., Cooper, J.C., Robertson, E.R., Gabrieli, J.D.E., Gross, J.J., 2005. Individual differences in trait rumination and the neural systems supporting cognitive reappraisal. Cogn Affect Behav Neurosci 5 (2), 156–168.

Raymaekers, S., Luyten, L., Bervoets, C., Gabriëls, L., Nuttin, B., 2017. Deep brain stimulation for treatment-resistant major depressive disorder: a comparison of two targets and long-term follow-up. Transl. Psychiatry 7 (10), e1251.

Razi, A., Seghier, M.L., Zhou, Y., McColgan, P., Zeidman, P., Park, H.-J., Sporns, O., Rees, G., Friston, K.J., 2017. Large-scale DCMs for resting-state fMRI. Netw Neurosci 1 (3), 222–241.

Rogers, M.A., Kasai, K., Koji, M., Fukuda, R., Iwanami, A., Nakagome, K., Fukuda, M., Kato, N., 2004. Executive and prefrontal dysfunction in unipolar depression: a review of neuropsychological and imaging evidence. Neurosci. Res. 50 (1), 1–11.

Rolls, E.T., 2015. Limbic systems for emotion and for memory, but no single limbic system. Cortex 62, 119–157.

Schlösser, R.G.M., Wagner, G., Koch, K., Dahnke, R., Reichenbach, J.R., Sauer, H., 2008. Fronto-cingulate effective connectivity in major depression: a study with fMRI and dynamic causal modeling. Neuroimage 43 (3), 645–655.

Seeley, W.W., Menon, V., Schatzberg, A.F., Keller, J., Glover, G.H., Kenna, H., Reiss, A.L., Greicius, M.D., 2007. Dissociable intrinsic connectivity networks for salience processing and executive control. J. Neurosci. 27 (9), 2349–2356.

Sejnowski, T.J., 1976. On global properties of neuronal interaction. Biol. Cybern. 22 (2), 85–95.

Sheehan, D.V., Lecrubier, Y., Sheehan, K.H., Amorim, P., Janavs, J., Weiller, E., Hergueta, T., Baker, R., Dunbar, G.C., 1998. The Mini-International Neuropsychiatric Interview (M.I.N.I.): the development and validation of a structured diagnostic psychiatric interview for DSM-IV and ICD-10. J. Clin. Psychiatry 59, 22–33.

Siegle, G.J., Steinhauer, S.R., Thase, M.E., Stenger, V.A., Carter, C.S., 2002. Can't shake that feeling: event-related fMRI assessment of sustained amygdala activity in response to emotional information in depressed individuals. Biol. Psychiatry 51 (9), 693–707.

Singh, M.F., Braver, T.S., Cole, M.W., Ching, ShiNung, 2020. Estimation and validation of individualized dynamic brain models with resting state fMRI. Neuroimage 221, 117046.

Smith, R.E., Tournier, J.-D., Calamante, F., Connelly, A., 2012. Anatomically-constrained tractography: Improved diffusion MRI streamlines tractography through effective use of anatomical information. Neuroimage 62 (3), 1924–1938.

Sokolov, A.A., Zeidman, P., Razi, A., Erb, M., Ryvlin, P., Pavlova, M.A., Friston, K.J., 2020. Asymmetric high-order anatomical brain connectivity sculpts effective connectivity. Network Neurosci. 4 (3), 871–890.

Sporns, O., 2014. Contributions and challenges for network models in cognitive neuroscience. Nat. Neurosci. 17 (5), 652–660.

Stephan, K., Iglesias, S., Heinzle, J., Diaconescu, A., 2015. Translational perspectives for computational neuroimaging. Neuron 87 (4), 716–732.

Stephan, K.E., Penny, W.D., Moran, R.J., den Ouden, H.E.M., Daunizeau, J., Friston, K.J., 2010. Ten simple rules for dynamic causal modeling. Neuroimage 49 (4), 3099–3109.

Steriade, M., McCormick, D., Sejnowski, T., 1993. Thalamocortical oscillations in the sleeping and aroused brain. Science 262 (5134), 679–685.

Surguladze, S., Brammer, M.J., Keedwell, P., Giampietro, V., Young, A.W., Travis, M.J., Williams, S.C.R., Phillips, M.L., 2005. A differential pattern of neural response toward sad versus happy facial expressions in major depressive disorder. Biol. Psychiatry 57 (3), 201–209.

Thompson, S.M., Kallarackal, A.J., Kvarta, M.D., Van Dyke, A.M., LeGates, T.A., Cai, X., 2015. An excitatory synapse hypothesis of depression. Trends Neurosci. 38 (5), 279–294.

Timofeev, I., Bazhenov, M., 2005. In: Mechanisms and biological role of thalamocortical oscillations. *Trends in chronobiology research.* Nova Science Publishers Inc., pp. 1–47

Tong, Y., Hocke, L.M., Frederick, B.B., 2019. Low frequency systemic hemodynamic "noise" in resting state BOLD fMRI: characteristics, causes, implications, mitigation strategies, and applications. Front. Neurosci. 13, 787.

Tournier J, Calamante F, Connelly A (2010) Improved probabilistic streamlines tractography by 2nd order integration over fibre orientation distributions. In: Proc 18th Annual Meeting of the Intl Soc Mag Reson Med (ISMRM), Stockholm, Sweden. p 1670.

Tulving, E., Markowitsch, H.J., 1998. Episodic and declarative memory: role of the hippocampus. Hippocampus 8 (3), 198–204.

Vincent, J.L., Kahn, I., Snyder, A.Z., Raichle, M.E., Buckner, R.L., 2008. Evidence for a frontoparietal control system revealed by intrinsic functional connectivity. J. Neurophysiol. 100 (6), 3328–3342.

Vyas, A., Mitra, R., Shankaranarayana Rao, B.S., Chattarji, S., 2002. Chronic stress induces contrasting patterns of dendritic remodeling in hippocampal and amygdaloid neurons. J. Neurosci. 22 (15), 6810–6818.

Wang, M., Yang, P., Wan, C., Jin, Z., Zhang, J., Li, L., 2018. Evaluating the role of the dorsolateral prefrontal cortex and posterior parietal cortex in memory-guided attention with repetitive transcranial magnetic stimulation. Front. Hum. Neurosci. 12, 236.

Wang, P., Kong, R., Kong, X., Liégeois, R., Orban, C., Deco, G., van den Heuvel, M.P., Thomas Yeo, B.T., 2019. Inversion of a large-scale circuit model reveals a cortical hierarchy in the dynamic resting human brain. Sci. Adv. 5 (1), eaat7854.

Wilson, H.R., Cowan, J.D., 1972. Excitatory and inhibitory interactions in localized populations of model neurons. Biophys. J. 12 (1), 1–24.

Yan, C.-G., Chen, X., Li, L.e., Castellanos, F.X., Bai, T.-J., Bo, Q.-J., Cao, J., Chen, G.-M., Chen, N.-X., Chen, W., Cheng, C., Cheng, Y.-Q., Cui, X.-L., Duan, J., Fang, Y.-R., Gong, Q.-Y., Guo, W.-B., Hou, Z.-H., Hu, L., Kuang, L.i., Li, F., Li, K.-M., Li, T., Liu, Y.-S., Liu, Z.-N., Long, Y.-C., Luo, Q.-H., Meng, H.-Q., Peng, D.-H., Qiu, H.-T., Qiu, J.,

Shen, Y.-D., Shi, Y.-S., Wang, C.-Y., Wang, F., Wang, K., Wang, L.i., Wang, X., Wang, Y., Wu, X.-P., Wu, X.-R., Xie, C.-M., Xie, G.-R., Xie, H.-Y., Xie, P., Xu, X.-F., Yang, H., Yang, J., Yao, J.-S., Yao, S.-Q., Yin, Y.-Y., Yuan, Y.-G., Zhang, A.-X., Zhang, H., Zhang, K.-R., Zhang, L., Zhang, Z.-J., Zhou, R.-B., Zhou, Y.-T., Zhu, J.-J., Zou, C.-J., Si, T.-M., Zuo, X.-N., Zhao, J.-P., Zang, Y.-F., 2019. Reduced default mode network functional connectivity in patients with recurrent major depressive disorder. PNAS 116 (18), 9078–9083.

Yan, C.G., Zang, Y.F., 2010. DPARSF: A MATLAB Toolbox for "Pipeline" data analysis of resting-state fMRI. Front. Syst. Neurosci. 4, 13.

Zalesky, A., Fornito, A., Bullmore, E.T., 2010. Network-based statistic: identifying differences in brain networks. Neuroimage 53 (4), 1197–1207.